# Dynamical properties of Hamiltonian Systems. Applications to Celestial Mechanics [1]

Carles Simó
Departament de Matemàtica Aplicada i Anàlisi
Universitat de Barcelona, Barcelona, Catalunya
carles@maia.ub.es

# 1 Introduction

Our goal is to study some properties of the *dynamics of the N-body problem*. As it is well known, the *Newtonian model of N punctual masses*, $m_i, i = 1, \ldots, N$, located at $q_i(t) \in \mathbb{R}^d$, moving under their mutual gravitational attraction is described by the equations

$$\ddot{q}_i = \sum_{j=1, j\neq i}^{N} (q_j - q_i)/r_{i,j}^3, \quad r_{i,j}^2 = ||q_j - q_i||_2^2, \quad i = 1, \ldots, N. \tag{1}$$

The system has several *first integrals*. The centre of mass ones, in a suitable reference moving linearly with constant velocity, are $\sum_{i=1}^N m_i q_i = 0$, $\sum_{i=1}^N p_i = 0$, where the related momenta are defined as $p_i = m_i \dot{q}_i$. Furthermore, defining the kinetic energy as $T(p) = \sum_{i=1}^N ||p_i||_2^2/m_i$ and the potential one as $U(q) = \sum_{1\leq i<j\leq N} m_i m_j / r_{i,j}$ one has the energy integral $T(p) - U(q) = H(q,p) = h$. The total angular momentum $\sum_{i=1}^N m_i q_i \wedge \dot{q}_i$ is another first integral. In general no more first integrals exist. Of course, $q$ and $p$ above refer to the vectors in $\mathbb{R}^{Nd}$ which contain all the components of positions and momenta. System (1) can be put in *Hamiltonian formulation*: $\dot{q}_i = \partial H/\partial p_i$, $\dot{p}_i = -\partial H/\partial q_i$. The pairs $(q_i, p_i)$ are canonically conjugated. In present case the Hamiltonian has $Nd$ degrees of freedom (dof), despite the use of the centre of mass integrals reduces to $(N-1)d$ and the angular momentum gives additional reduction. For the applications we shall consider the cases $d = 2$ and $d = 3$. The equations are analytic except on the collision set, when at least one of the values of $r_{i,j}$ equals zero.

In many problems it is interesting to consider that some of the bodies have a negligible mass. They are influenced by the massive bodies but have no action on them. These are the *restricted* $N$-body problems.

The $N$-body problem belongs to the general class of Hamiltonian systems. In these systems and in all kinds of dynamical systems, the ultimate goal is *to describe the main mechanisms leading to a fairly global description of the dynamics*, how it depends on parameters and, if it is possible to act on the system (either with additional forces or by changing parameters) how to have some control on the behaviour of the system. In present case we shall be interested in *conservative systems*, either in the continuous version described by a Hamiltonian or in the discrete version. Next we make some comments on the passage from continuous systems to discrete ones and vice versa.

## 1.1 Continuous and discrete conservative systems

The associated discrete version is given by *symplectic maps*: $F : (x, y) \to (X, Y)$, where $X = F_1(x, y)$, $Y = F_2(x, y)$, with $x, y, X, Y$ belonging to some set in $\mathbb{R}^d$ and such that the 2-form $dx \wedge dy = \sum_{i=1}^d dx_i \wedge dy_i$ is preserved: $dX \wedge dY = dx \wedge dy$. We can replace working in $\mathbb{R}^d \times \mathbb{R}^d$ by a formulation in symplectic manifolds but, to have a simpler presentation, we prefer to work explicitly using coordinates and refrain from extensions.

It is a simple matter to obtain discrete maps from a flow leaded by $\dot{x} = f(x)$, where $f$ is a vector field (v.f.) in some open set $U$ of $\mathbb{R}^n$. Assume $\Sigma$ is an hypersurface, given as the points $x \in U$ such that $g(x) = 0$, where $g : U \to \mathbb{R}$. We require that is satisfies the *transversality condition*. We say that $\Sigma$ is transversal to the v.f. if the scalar product $(f, \nabla g)$ is different from zero in $\Sigma$. The geometrical meaning is clear: the flow of $f$ (that we shall denote as $\varphi_t^f$ or simply as $\varphi_t$) crosses transversally the section $\Sigma$. In

[1] Text of the lectures delivered at the Centre de Recerca Matemàtica on January 27-31, 2014.

many examples one simply takes as $g$ one of the coordinates (either equal to zero or to a constant). In that case $\Sigma$ is usually not the full coordinate hyperplane, but the part of it satisfying the transversality condition. Then, given a point $Q \in \Sigma$ we define a map, the so-called *Poincaré map* $\mathcal{P}$, as the first return of $Q$ to $\Sigma$: $\varphi_{t(Q)}(Q) \in \Sigma$ with a minimal value of $t(Q) > 0$. Note that, eventually, some $Q$ can never return to $\Sigma$ for any $t > 0$. This implies that $\Sigma$ has to be reduced to a suitable subset. We also note that the return time $t(Q)$ depends on the starting point. We denote as $\mathcal{P}(Q) := \varphi_{t(Q)}(Q)$ the image of $Q$ under the Poincaré map $\mathcal{P}$.

In the case of a Hamiltonian $H$ with $m$ dof (hence $x$ has dimension $2m$) fixing a transversal section $\Sigma$ and the level of energy $h$, the Poincaré map associated to $\Sigma$ defines a map in $\Sigma \cap H^{-1}(h)$, of even dimension $2(m-1)$. This map is symplectic.

Given a discrete map $x \to F(x)$ in $V \subset \mathbb{R}^n$ there is also a simple way to produce a v.f. such that it has, as associated Poincaré map, the initial map, provided $F$ is close to the identity, say $F(x) = x + \varepsilon G(x)$ with $\varepsilon$ small enough (see later). For concreteness we shall assume that $G$ is a real analytic function. We want to define a non-autonomous periodic v.f. of period 1 in $t$. Let us consider, for instance, and for a given $k > 1$, the function $\psi_k(t) = c \int_0^t s^k (1-s)^k \, ds$, where the constant $c$ is selected to have $\psi_k(1) = 1$. Then we define the flow starting at the point $x$ after a time $t \in [0,1]$ as $\varphi_t(x) = x + \varepsilon \psi_k(t) G(x)$, that is, we are using an Hermite-like interpolation, because $\psi_k^j(0) = 0$ for $j = 0, \ldots, k$, $\psi_k(1) = 1$ and $\psi_k^j(1) = 0$ for $j = 1, \ldots, k$. Other interpolations can also be used. For other values of $t$ it is defined by periodicity: $\varphi_t(x) = \varphi_{(t)}(x)$ where $(t) = t - [t]$, being $[t]$ the largest integer less than or equal to $t$. Clearly $\varphi_0(x) = x$, $\varphi_1(x) = F(x)$. Now we should define the v.f. at $(y, \tau)$ for $\tau \in [0,1]$. To this end we look for $z$ such that $\varphi_\tau(z) = y$. It follows immediately, from the implicit function theorem, that a solution exists if $|| \operatorname{Id} + \varepsilon DG||_\infty > 0$. Finally the v.f. is $f(y, \tau) = \varepsilon \frac{d\psi_k}{dt}(\tau) G(z)$.

We note that this is a slow v.f., having the parameter $\varepsilon$ as a factor. It is usually denoted as the *suspension* of the map $F$. We can consider if it is possible to approximate it by an autonomous v.f. This follows from a general theorem on averaging, that we present in a wider context: the case of v.f. depending on time in a quasiperiodic way.

**Theorem 1.1.** *Let*

$$\dot{z} = \varepsilon f(z, \theta, \varepsilon), \tag{2}$$

*where $f$ is analytic in $(z, \theta)$ for $z \in \Omega \subset \mathbb{C}^n$, $\Omega = D + \Delta$, a $\Delta$-neighbourhood of $D$ in $\mathbb{C}^n$, $D$ a compact in $\mathbb{R}^n$ and $\theta \in \mathbb{T}^p + \Delta$, $p \geq 2$, where $\mathbb{T}^p$ is a $p$-dimensional torus. Assume $f$ in (2) is bounded in $\varepsilon$ for $|\varepsilon| \leq \varepsilon_0$ and $\theta = \omega t$, where $\omega \in \mathbb{R}^n$ is a vector of frequencies satisfying the Diophantine condition (DC)*

$$|(k, \omega)| \geq b |k|^{-\tau}, \quad \forall k \in \mathbb{Z}^p \setminus \{0\}, \tag{3}$$

*where $b > 0$, $\tau > p - 1$ and $|k| = \sum_{i=1}^p |k_i|$. Then, if $\varepsilon_0$ is small enough, for a fixed $\varepsilon$ with $|\varepsilon| \leq \varepsilon_0$, there exists a change of variables $z = h(w, \theta, \varepsilon)$, analytic in $(w, \theta)$ for $w \in D + \Delta/2$, $\theta \in \mathbb{T}^p + \Delta/2$, such that the new equation is $\dot{w} = \varepsilon(g(w, \varepsilon) + r(w, \theta, \varepsilon))$ and the remainder satisfies an exponentially small bound*

$$|r|_{\Delta/2} < c_1 \exp(-c_2/\varepsilon^{c_3}), \tag{4}$$

*where $c_1, c_2 > 0, c_3 = 1/(\tau + 1)$. The constants $c_1$, $c_2$ depend only on $|f|_\Delta$, the dimensions and the constants in (3). Furthermore $|g|_{\Delta/2} < 2|f|_\Delta$. Here $|f|_\Delta$ denotes the sup norm of $f$ in $D + \Delta$, $\mathbb{T}^p + \Delta$ for the fixed value of $\varepsilon$.*

**Remarks**.

1) In the periodic case (it would be $p = 1, \tau = 0$), there is no need of analyticity wrt $t$. Just integrable is enough. Then $c_3 = 1$. See [33].

2) The optimal number of averaging steps (i.e., up to which order in $\varepsilon$ one should cancel the quasiperiodic dependence) is $\approx \varepsilon^{-c_3}$.

3) If $f$ is a Hamiltonian v.f. the change to $w$ can be made canonical. Hence, the averaged system, skipping the remainder $r$, is also Hamiltonian. See [47].

4) If $f$ has been obtained by suspension of a map $F$, we can produce an autonomous v.f., like $g$, which interpolates $F$ except by exponentially small terms.

The basic idea of the proof is to obtain the change $z = h(w, \theta, \varepsilon)$ by means of *sequence of changes*. This methodology is common to many topics in dynamical systems. First we try to cancel the *purely quasiperiodic* terms in $f$, that is, the terms in $\tilde{f} = f - \bar{f}$, where $\bar{f}$ denotes the average wrt $\theta$. Writing the suitable condition for the change one checks that one has to solve a PDE to obtain the quasiperiodic coefficients in this first change. To solve it with control on how the coefficients of the change behave is where the *analyticity wrt* $\theta$ and the DC (3) play its role. In the periodic case one has to do just an integration, and this is why to be integrable in $t$ is enough in that case.

Once the terms in $\tilde{f}$ have been skipped, one has to check the contribution that the change makes in $\varepsilon^2$. Here is where the *analyticity wrt* $z$ plays a role, to bound the derivatives in a slightly smaller strip, passing from half width $\Delta$ to $\Delta_1$. Then we proceed to cancel the purely quasiperiodic terms which appear with $\varepsilon^2$ as factor, and so on, to cancel the non-autonomous terms in $\varepsilon^k, k = 3, \ldots$. At every step, to be able to bound the contributions made by the change to higher order in $\varepsilon$, one has to reduce the size of the analyticity domain, introducing a decreasing sequence for the half widths of the successive domains $\Delta_2 > \ldots > \Delta_k > \ldots$.

After every change one has a bound on the remainder. If for a given $\varepsilon$ we do too many changes, as we want to keep an analyticity domain of positive half width, the differences $\Delta_{k-1} - \Delta_k$ are small. This implies bad estimates for the derivatives and an increase on the size of the remainder. This is why, for every $\varepsilon$, there is an optimal order. Simpler estimates give then the bound in (4). See [38] for details and examples.

These kind of bounds on remainders are relevant to bound errors on approximations done, for instance, with normal forms (see subsection 3.2). The variables can be scaled in the domain of interest and the role of $\varepsilon$ is played by the size of the domain.

Finally we stress that the passage from flows to maps and vice versa, when the map or some power of it is close enough to the identity, allows a more complete understanding and representation of key phenomena.

In what follows we shall consider that all v.f. and maps are in the analytic category.

## 1.2 Comments on the contents

Letting aside the two-body problem and subclasses with some special symmetry, the simplest $N$-body problem is the planar circular restricted three-body problem which has 2 dof (see section 4). Next simplest problem can be the planar general three-body problem. Even restricting to a fixed value of the angular momentum it has 3 dof. The dimension can be reduced by fixing energy and using a Poincaré section. In the first case we obtain symplectic 2D maps, easy to visualize. In the second case we have symplectic 4D maps, not so easy to visualize. There are key objects of codimension-1 (see subsection 3.4) and homoclinic/heteroclinic phenomena due to the intersection of two objects of dimension 2 in dimension 4. The invariant tori (see subsection 3.3) do not separate the phase space and slow escape from points as close as we like to invariant tori (Arnold diffusion or general diffusion, see subsection 3.5), avoiding a large set of nearby tori, can occur.

For these reason we devote section 2 to introduce several simple but paradigmatic examples in the 2D case, with the hope that will make easier to grasp the main ideas in higher dimension. See also slides 2. for several examples with low dimensional conservative systems.

Section 3 is devoted to present some general theoretical results. But it is also relevant to see how to use the ideas of the proofs in concrete examples. In many cases the effective computation is based on the implementation of the proof, either by symbolical or numerical methods or, quite frequently, by a combination of both.

Finally section 4 presents some applications to Celestial Mechanics, with a variety of goals.

Concerning references, most of the basic results can be found in classical standard books. A few of them appear in the list of references, and no explicit mention to them is made in the text. Some references to concrete topics are scattered along the text and they are given at the end of these notes.

The reader can also look, at the end of the references, at the list of slides of several talks given in the past and that, in turn, refer to some animations.

# 2 Low dimension: Same key examples of 2D symplectic maps to see the kind of phenomena to face

Invariance of $dx \wedge dy$ in dimension 2 is equivalent to area preservation. We shall denote as APM the Area-Preserving Maps. The simplest non-trivial APM which come to mind are the quadratic ones: $x, y \in \mathbb{R}$ and $F_1, F_2$ are polynomials of degree two. These maps were widely studied by M. Hénon [19]. See also slides 5. and slides 7. They are relevant because

1) The number of parameters can be reduced to only one, and they have a very simple geometrical interpretation.
2) They appear in a natural way as a very good approximation in some parts of $\mathbb{R}^2$ when we consider arbitrary APM. In particular when we study Poincaré maps of Hamiltonian systems with 2 dof.
3) Many problems concerning: a) the existence of invariant curves diffeomorphic to $\mathbb{S}^1$; b) the role of the invariant manifolds of hyperbolic fixed or periodic points and how they lead to the existence of chaos, and c) the geometrical mechanisms leading to the destruction of invariant curves, can all be understood thanks to our knowledge of the quadratic case.

We shall illustrate some of these features in that section.

## 2.1 The Hénon map

In the initial formulation the map (except in some degenerate cases) can be written, thanks to the APM character, shift of origin and scaling, as $F : (x, y) \to (1 - ax^2 + y, -x)$. Hence, this family of maps depends on a single parameter, $a$. The geometric interpretation is simple: it is the composition of the map $(x, y) \to (x, y + 1 - ax^2)$ (one of the so-called de Jonquières maps) and a rotation of angle $-\pi/2$. Figure 1 shows, for $a = -1/2$, the square $[-3, 3]^2$ (in red), the first image (in green) and part of the next two images (in blue and magenta, respectively). One can ask whether all points will escape for future iterations. To give an answer to this question, we plot in black the set of points which remain bounded for all iterations and the selected value of $a$.

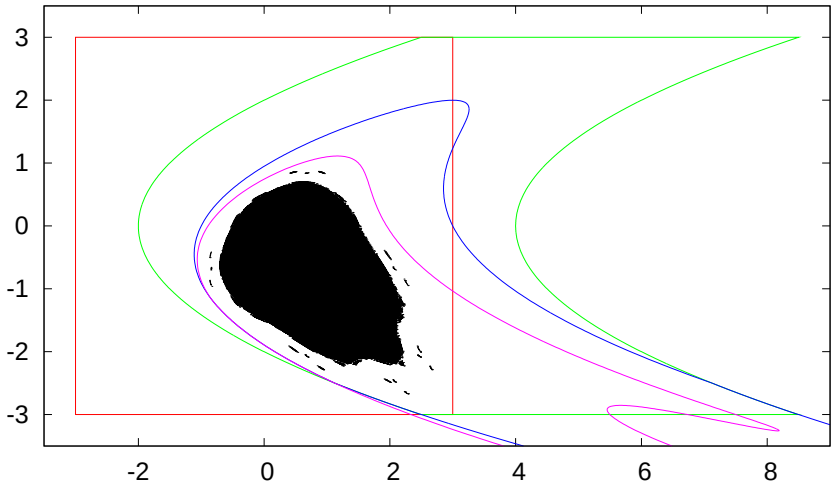


Figure 1: The square $[-3, 3]^2$ (in red) and the first three images of it under the Hénon map with $a = -0.5$, shown in green, blue and magenta, respectively. The last two have parts outside the frame shown here. In black we display the invariant set of points which remain bounded under all iterations.

However we shall use another representation of that map, see [48], given by

$$F_c \begin{pmatrix} x \\ y \end{pmatrix} \to \begin{pmatrix} x + 2y + \frac{c}{2}(1-(x+y)^2) \\ y + \frac{c}{2}(1-(x+y)^2) \end{pmatrix}, \tag{5}$$

which depends on $c$ that can be assumed to be positive. It has two fixed points: $H$ at $(-1,0)$, hyperbolic $\forall c > 0$, and $E = (1,0)$, elliptic for $0 < c < 2$ and hyperbolic with reflection for $c > 2$. The reversor $S(x,y) = (x,-y)$ allows to obtain $F_c^{-1} = SF_cS$.

Doing the change of scale $(\xi,\eta) = (x, 2y/\sqrt{c})$ one obtains a map $\sqrt{c}$-close to the identity. According to section 1 it can be approximated by the time-$\sqrt{c}$ flow of the v.f. $d\xi/dt = \eta$, $d\eta/dt = 1-\xi^2$, with Hamiltonian $K(\xi,\eta) = \eta^2/2 - \xi + \xi^3/3$. It is, of course, a trivial matter to improve $K$ to any power of $\sqrt{c}$. This v.f. has the same fixed points as $F_c$ and a separatrix on the level $K = 2/3$.

Next we show iterates of some initial points under $F_c$ for $c = 0.2$ and $c = 0.762$.

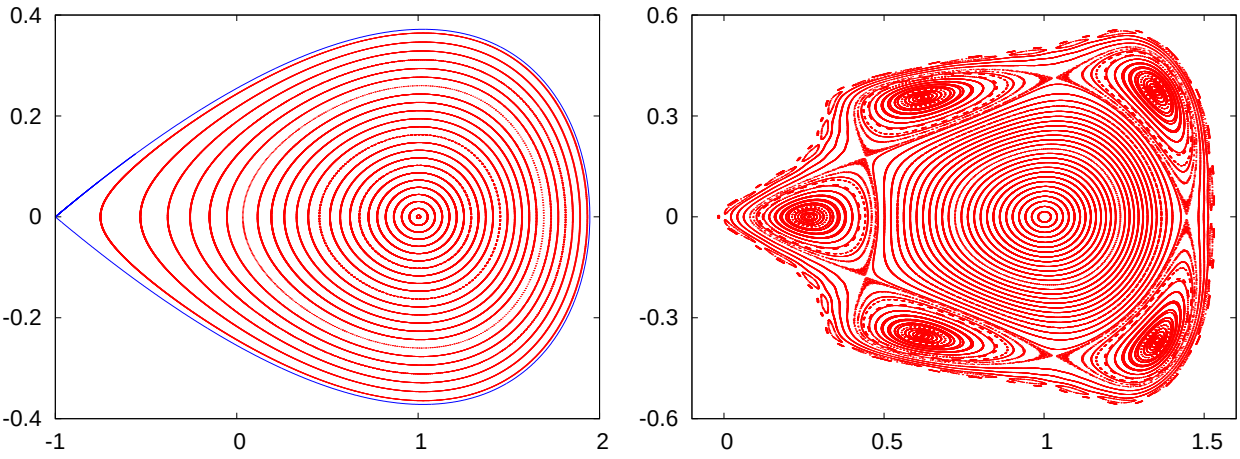


Figure 2: Some iterates under $F_c$. Left: for $c = 0.2$. Right: for $c = 0.762$. We have taken initial points on $y = 0$ and plotted 5,000 iterates of each one after a transient of $10^6$ iterates. Points outside the displayed domain escape to infinity close to the left branch of $W^u_H$.

An important characteristics of points whose orbit is an invariant curve (IC) is the *rotation number* $\rho$. It measures the average value of the fraction of revolution that the point turns in each iterate. We can look at the curves around the elliptic point $E$ in the previous plots and take polar coordinates. Let $\theta_k$ the angle of the $k$-th iterate, but considered in the lift $\mathbb{R}$ instead of $\mathbb{S}$. Note that in this example the points turn clockwise. Then we define

$$\rho = \frac{1}{2\pi} \lim_{k\to\infty} \frac{\theta_k}{k}. \tag{6}$$

It always exists and does not depend on the initial point on the curve.

On the left plot one can see a pattern which looks like the phase portrait of a 1 dof Hamiltonian, with a foliation by periodic solutions and a separatrix in blue. It seems that, as in the case of 1 dof systems the map is *integrable*. That is, there exists a non-constant function $C(x,y)$ preserved by the map: $C(F(x,y)) = C(x,y)$. In fact there is a Cantor set (of positive measure) of IC with $\rho \notin \mathbb{Q}$, an infinite number of periodic orbits of elliptic and hyperbolic type and the right hand sides of the manifolds of $H$ do not coincide. What happens is that the differences wrt the flow case are extremely small, in agreement with (4). We shall see details on the smallness in section 2.1.2.

The right plot displays a typical behaviour of a *not close to integrable APM*. Certainly there are many IC (again a Cantor set) around the point $E$, but at some distance one can see big *period-5 islands* around elliptic periodic points of period 5 and one can guess the existence of period-5 hyperbolic points. Close to them there are *chaotic orbits*, still surrounded by some more IC (rotational, that is, they make the full turn around $E$) and, finally, some little islands before reaching a place where most of the points *escape*.

### 2.1.1 Some comments on invariant curves

The plots in Figure 2 raise several questions:

1) Do really IC exist for $F_c$?
2) Which is the structure of the set of IC?
3) How are they destroyed?
4) What happens after its destruction?

First we introduce the so-called *twist maps*. These are integrable maps defined in some annular domain $r_d < r < r_u$, having a foliation by IC, given by

$$T(r, \alpha) = (r, \alpha + a(r)) \tag{7}$$

and satisfying the *twist condition*

$$da(r)/dr \neq 0 \tag{8}$$

Of course, one can have the form (7) after a diffeomorphism. The curves can have a shape different from circles, like ellipses, to be star-shaped or not.

A key result is *Moser twist theorem*.

**Theorem 2.1.** *Consider a perturbation $F_\varepsilon = T + \varepsilon P$ of a twist map $T$. Then, if we have an invariant curve of $T$ which has Diophantine rotation number $\gamma$, this curve, with a small deformation, subsists for $F_\varepsilon$ provided $\varepsilon$ is sufficiently small.*

The Diophantine condition, in present case, is like (3) with frequencies $\gamma$ and 1: $|k_1\gamma + k_0| \geq b|k|^{-\tau}$, $\forall (k_1, k_0) \in \mathbb{Z}^2 \setminus \{0\}$, where $|k|$ denotes some norm of $k = (k_1, k_0)$.

Let us comment a little on the three conditions: a) it must be a perturbation of a twist map $T$; b) the rotation number $\gamma$ must be Diophantine; c) it must be close enough to $T$, that is, $\varepsilon$ must be small.

Assume that the Fourier representation of the IC of $T$ which has $\rho = \gamma$ is $r(\alpha) = \sum_{j\in\mathbb{Z}} a_j \exp(\mathrm{i}\, j\alpha)$ in the present polar coordinates we are using (typically, for a given problem, the twist map will not be given in the form (7) and to put explicitly it in this form can be cumbersome). Let $r_\varepsilon(\alpha) = \sum_{j\in\mathbb{Z}} b_j \exp(\mathrm{i}\, j\alpha)$ be the representation of the desired IC, invariant under $F_\varepsilon$. The invariance condition is expressed, in $(r, \alpha)$ as $F_\varepsilon(r_\varepsilon(\alpha), \alpha) = (r_\varepsilon(\alpha + 2\pi\gamma), \alpha + 2\pi\gamma)$. It is clear that we can fix the origin of angles in an arbitrary way.

We try to pass from the coefficients $a_j$ to the $b_j$ by making a sequence of changes (similar to the case of theorem 1.1) such that after the $k$-th change, one has an approximation of the IC under $F_\varepsilon$ with $\rho = \gamma$ with an error $\mathcal{O}(\varepsilon^{2^k})$. That is, a Newton method in the space of Fourier series. The equation to be solved at each step is of the form $G(\alpha + 2\pi\gamma) - G(\alpha) = R(\alpha)$, the so called *homological equation*, where $R(\alpha)$ is related to the error of the previous approximation and has zero average, a necessary condition in order to be possible to solve the equation.

Using Fourier representations for $G$ and $R$: $G = \sum_{j\in\mathbb{Z}} g_j \exp(\mathrm{i}\, j\alpha), R = \sum_{j\in\mathbb{Z}} r_j \exp(\mathrm{i}\, j\alpha), r_0 = 0$, it is straightforward to obtain $g_j = r_j/(\exp(\mathrm{i}\, j2\pi\gamma) - 1), j \neq 0$. But, of course, if $j\gamma$ is close to an integer, the previous denominator is close to zero. This is known as the *small denominators problem*. The DC allows us to control the behaviour of the coefficients of $G$, so that if $R$ is analytic in some complex strip around real values of $\alpha$, $G$ is also analytic (perhaps in a slightly narrower strip).

The problem is then that the error in the next approximation does not have zero average and we will not be able to solve the next homological equation. But this average can be canceled by modifying the initial independent term $a_0$ (or, equivalently, by selecting a proper value for $g_0$) and this is possible thanks to the twist condition by applying the implicit function theorem. It is convenient to express the twist condition as $d\rho/da_0 \neq 0$; that is, in terms of the average of the initial curve. Finally the smallness of $\varepsilon$ is necessary to have convergence in the Newton procedure. Note that, for a fixed $\gamma$, the larger the twist condition, the larger are the admissible values of $\varepsilon$.

In section 3.3 we shall talk about generalizations to higher dimension, both for symplectic maps and for Hamiltonian flows. The key ideas for the proofs are the same.

Using *normal form* tools (see section 3.2) it is easy to prove that, what seem IC in Figure 2 are really IC, at least close to the point $E$. Furthermore, it is clear that the structure of the set of IC is Cantorian, because so is the structure of the set of Diophantine numbers for values of $b, \tau$ bounded from below, see (3).

It is interesting to see what happens when the twist condition is *not satisfied*. Figure 3 shows, for the map (5), with $c = 1.35$, the evolution of $\rho$ as a function of $x$ for initial points of the form $(x, 0)$. It is clear that $\rho$ is only defined for IC and periodic orbits (or islands) and in present case it seems that this occurs for most of the initial values of $x$. One can prove that this behaviour, with a local minimum at $x = 1$ and one local maximum on each side, appears only for $c \in (c_1, c_2)$, $c_1 = 5/4$, $c_2 \approx 1.4123$. For $c \in (0, c_1)$ one has a local (in fact, global) maximum at $x = 1$ (the point $E$).

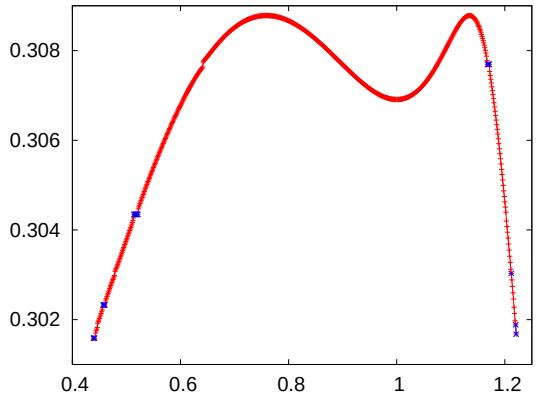


Figure 3: For $c = 1.35$ the value of $\rho = \rho(x)$ is plotted for initial points on $y = 0$. In blue the points with $\rho \in \mathbb{Q}$. Note that now, to the left or to the right of $x = 1$ the function $\rho$ is no longer monotonous.

The twist condition is lost near the maxima. Let $\rho_M$ be the value of $\rho$ at a given maximum $M$. Assume that there exist rationals $p/q < \rho_M$ with $q$ not too large. They give rise to the typical islands structure, with $q$ islands on each family, on both sides of the IC with $\rho = \rho_M$ (or close to it). The interaction of these two families of islands, with $\rho = p/q$, gives rise to the so-called *meandering curves*, see [40], which cannot be written with the radius as a function of the angle seen from the point $E$. The curves have some folds (or meanders) but it is still possible to apply Moser theorem 2.1 to prove that they exist.

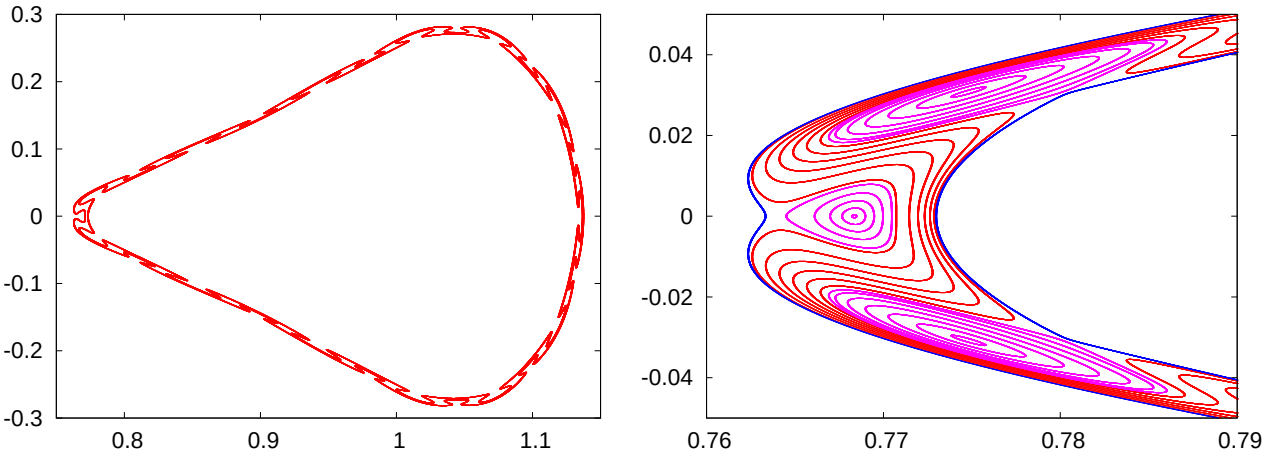


Figure 4: Left: We show a couple of orbits for $c = 1.3499$, sitting on a domain in which $\rho$ passes through a maximum. These orbits are on invariant curves known as meanders. Right: A magnification of the left. Beyond different meanders in red, one can see two typical invariant curves (inner and outer) in blue and islands, in magenta, which belong to two different chains of islands of rotation number 4/13.

### 2.1.2 Some comments on invariant manifolds of hyperbolic points

Beyond the IC of an APM there are other very important invariant objects which play a key role in dynamics (this is also true for more general maps and flows in any dimension, see section 3.4). They are the *stable and unstable manifolds of the hyperbolic fixed or periodic points*. They can be seen as the non-linear generalisation of the invariant subspaces of the differential of the map at the fixed point. On the left plot in Figure 2, for $c = 0.2$, the branches $W^{u,+}$ and $W^{s,-}$ (the ones which start to the right of $x = -1$) seem to be coincident but they are not. Figure 5, left, shows a magnification when they return to the vicinity of the point $(-1, 0)$, after going clockwise around $E$ under $F_c$ (red points) or counterclockwise under $F_c^{-1}$ (blue points). We see tiny oscillations with a size $\mathcal{O}(10^{-3})$. The right plot in Figure 5 shows the manifolds for $c = 0.77$ with large oscillations. The points in $W^u \cap W^s$ are known as *homoclinic points* (or biasymptotic points). Some of them, on $y = 0$, can be seen to the right of the plot. The successive nearby returns of the manifolds produce infinitely many homoclinic points. Depending on the location of a point wrt a given homoclinic, after passing close to $H$ under iteration by $F_c$ will follow close to the positive, $W^{u,+}$, or to the negative, $W^{u,-}$, branches of $W^u$. Similar for the stable branches using $F_c^{-1}$.

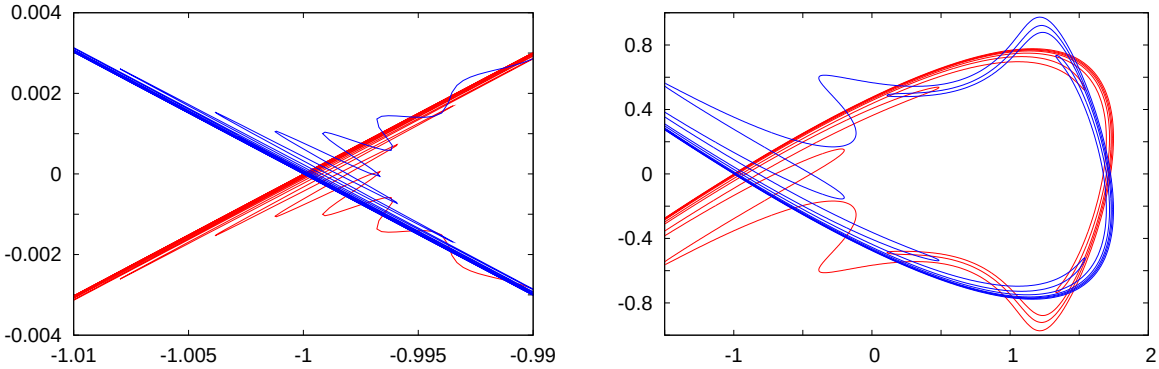


Figure 5: Left: a magnification of Figure 2 showing that the manifolds do not coincide. Right: part of the invariant manifolds of the hyperbolic point $H$ for $c = 0.77$ (the unstable manifold in red, the stable in blue). One has $W_H^s = S(W_H^u)$. The splitting of the manifolds is now clearly visible. It is increasing with $c$. Note that the domain around the point $E$ which is not covered by the oscillations of the manifolds, becomes smaller. Compare with the non-escaping set of points in Figure 2 right, for a nearby value of $c$.

A measure of the lack of coincidence of $W^u$ and $W^s$ is the *splitting angle*. This is defined as the angle between the manifolds at a given homoclinic point. In the present case of quadratic APM, we can measure the angle at the first intersection of the manifolds with $y = 0$ to the right of $x = 1$ and see how it behaves as a function of $c$. For concreteness we denote this angle as $\sigma(c)$. In Figure 6, left and middle, we represent the value of $\sigma(c)$ in different scales. In the left plot, despite the splitting is different from zero for any $c > 0$, we see that only for $c > 0.2$ does it start to be visible. To make visible what happens for small $c$, we display, in the middle plot, $\log(\sigma)$ against $\log(c)$. Note that already for $c = 0.05$ the value of $\sigma(c)$ is below $10^{-15}$ and, hence, it is negligible for any practical application.

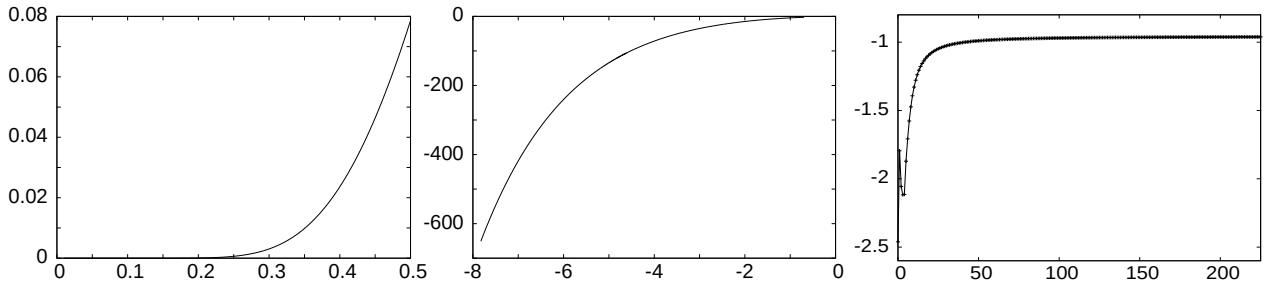


Figure 6: Different representations of the splitting angle $\sigma(c)$ between the manifolds at the first intersection with $y = 0, x > 1$. Left: $\sigma$ as a function of $c$, showing that $\sigma$ seems negligible for $c < 0.2$. At that value of $c$ one has $\sigma(c) = 6.21463426856826630097675406749853074250003\ldots \times 10^{-5}$. Middle: $\log(\sigma)$ as a function of $\log(c)$, which allows to see how small $\sigma(c)$ is for $c$ approaching zero. Right: the values of $\log_{10}(\omega_{2m}(2\pi^2)^{2m}/(2m+6)!)$ versus $m$, to give evidence of the Gevrey character of $\Omega(h)$ (see text).

Concerning the right plot in Figure 6 we need some preliminaries. Let $\lambda(c)$ be the *dominant eigenvalue* at the point $H$, which is equal to $1+c+\sqrt{2c+c^2}$ for $F_c$. An essential parameter in the theoretical study of the problem is $h(c) = \log(\lambda(c))$, because using suitable representations of the manifolds, it is possible to show that the splitting has upper bounds of the form $\exp(-\eta/h)$, where $\eta$ is related to the *imaginary part of the singularity of the separatrix of the limit flow*, as mentioned before Figure 2. This type of result is true for general analytic APM close to the identity map, see [10, 11]. In fact, for the present problem one can prove a more precise result. The splitting angle has the form

$$\sigma(c) = \frac{9}{2} \times 10^6 \pi^2 h(c)^{-8} \exp\left(-\frac{2\pi^2}{h(c)}\right) \times \Omega(h). \tag{9}$$

The term $\Omega(h)$ can be expanded in powers of $h^2$: $\Omega(h) = \sum_{m\geq 0} \omega_{2m} h^{2m}$ and can be bounded by $\omega_0 + \mathcal{O}(h)$. The constant term can be determined numerically and the first digits of $\omega_0$ are 2.48931280293671. Note, however, that the series defining $\Omega(h)$ is divergent. But for every value of $h$ it provides a good approximation if we truncate the summation at the right place. There is numerical evidence that the series is of *Gevrey-1 class*.

A formal power series $\sum c_k t^k$ is said to be of Gevrey-$\beta$ class if the series $\sum c_k (k!)^{-\beta} t^k$ is convergent. We can compute the series $\sum_{m\geq 0} \omega_m h^{2m}/(2m)!$ obtained from $\Omega(h)$ using $\beta = 1$. From a numerical determination of $\Omega(h)$, for different values of $h$, one can obtain the coefficients $\omega_{2m}$. See [12] for methodology and examples. In the right plot in Figure 6 we display $\log_{10}(\omega_{2m}(2\pi^2)^{2m}/(2m+6)!)$ as a function of $m$, which seems to tend to a constant. This gives evidence of the Gevrey-1 character of $\Omega(h)$ we mentioned. But to prove this fact is an *open problem*.

### 2.1.3 On the destruction of invariant curves

As mentioned in section 2.1.1, if $\rho$ is too close to a rational (in the Diophantine sense) or if the twist condition is too weak or if the perturbation $\varepsilon$ wrt an integrable map is too large, the IC does not exist. These analytic properties also have a nice geometric interpretation.

To illustrate the mechanism leading to the destruction of IC we consider Figure 7. It has been produced for $c = 0.618$ (left) and $c = 0.63$ (right) and it only shows the left part of the set of points which have bounded orbits. The case of Figure 7 is similar to the one in Figure 2 right, but now the main islands are 6-periodic instead of 5-periodic.

On the left plot one can see medium size islands with $\rho = 3/19$ (one of them with its central elliptic point on $y = 0$) and two symmetrical islands, in the same family, with $\rho = 4/25$, as well as several satellite islands, then tiny islands (e.g., with $\rho = 17/107, 39/245, 11/69, 19/119, 21/131, 13/81, \ldots$) and IC. In particular some IC are still present between the two chains of medium size islands. Some other IC, surrounding the main period-6 islands (not displayed) appear as the rightmost curves shown.

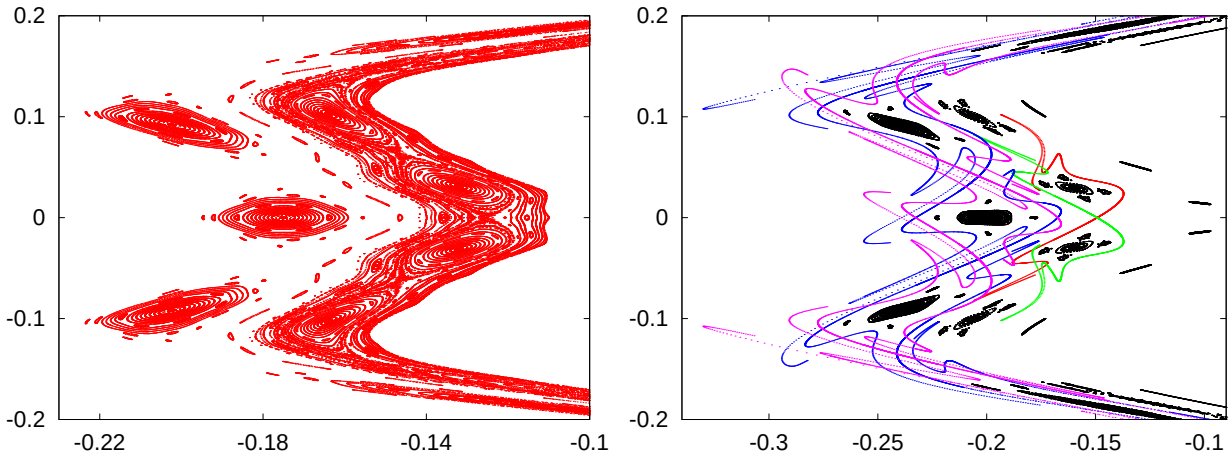


Figure 7: Left: A part of the set of non-escaping points for the map $F_c$ and $c = 0.618$. Right: similar plot for $c = 0.63$, displaying also several invariant manifolds of periodic hyperbolic points leading to heteroclinic intersections. See the text for details.

On the right plot we display in black two chains of islands of rotation numbers 3/19 and 4/25, corresponding to the ones in the left plot, but now they are smaller. Consider the associated hyperbolic periodic orbits, the one with rotation number 4/25 being visible on the $x$-axis and the two symmetric points belonging to the hyperbolic periodic orbit of rotation number 3/19 being close to $x = -0.2$ off the $x$-axis. The manifolds of these periodic orbits give rise to *heteroclinic connections* that is, intersections of the stable and unstable manifolds of two different objects. The manifolds $W^u_{4/25}, W^s_{4/25}$ are shown in red and green, respectively. The manifolds $W^u_{3/19}, W^s_{3/19}$ are shown in blue and magenta, respectively. Note that $W^u_{4/25}$ and $W^s_{3/19}$ (and, symmetrically $W^s_{4/25}$ and $W^u_{3/19}$) have *transversal* heteroclinic intersections. This produces an obstruction to the existence of the IC which could separate the chains of islands. This is the basis of the so-called *obstruction mechanism* [35].

Indeed, if we consider a curve formed by a piece of invariant manifold of the inner hyperbolic periodic point (the one of period 25) until the heteroclinic point, followed by a piece of invariant manifold of the outer hyperbolic periodic point (the one of period 19), from the heteroclinic point to the periodic one, the IC will have to cross it. This is impossible because of the invariance. In fact, one concludes that IC with $\rho \in (3/19, 4/25)$ cannot exist. But IC with $\rho$ in that interval are found for $c = 0.618$. Hence, the geometrical mechanism responsible for the destruction is the existence of heteroclinic connections which obstruct the possible curves.

Anyway, there are invariant objects with $\rho$ in the above mentioned interval. It is proved that they should be at the outer part of the manifolds of the hyperbolic periodic orbit with $\rho = 4/25$ and at the inner part of the manifolds of the hyperbolic periodic orbit with $\rho = 3/19$. The heteroclinic intersections of these manifolds create *gaps* which forbid the existence of points of the invariant object in them. As a consequence, the invariant object which remains is a *Cantor set* [28, 29]. Points which were located inside an IC for $c = 0.618$ and, hence, without being possible the escape, can now, for $c = 0.63$ find a gap of the Cantor set and escape under iteration. It looks like some random process and, certainly, the probabilities are related to the size of the gaps in the Cantor set.

## 2.2 The standard map

Looking at the right plot in Figure 2 we clearly see the period-5 islands around period-5 elliptic points and, as already said, we can guess the existence of period-5 hyperbolic points. We also see IC close to the island. Some of them inside, which have $\rho > 1/5$, and other outside, which have $\rho < 1/5$. If instead of iterations under $F_c$ we iterate using $F_c^5$ we will check that the inside curves turn a little clockwise and the outside ones turn a little counterclockwise. We can ask: what happens for an APM if we have two IC turning by iteration an small amount in opposite directions?

This is the contents of the so-called *last geometric theorem by Poincaré*. Between the two curves invariant, under a map $M$, should appear fixed points, generically isolated and alternatively elliptic and hyperbolic. Typically it appears one point of each type. But if the map is the $q$-th power of some other map $\tilde{M}$, with rotation number $p/q, (p, q) = 1$ then there are $q$ fixed points of each type under $M$, which are $q$-periodic under $\tilde{M}$.

The structure of the islands is reminiscent of the phase portrait of a pendulum, whose Hamiltonian is $H(x, y) = y^2/2 + \cos(x)$ using suitable coordinates. From a quantitative point of view (the width of the islands) we recall that the maximal distance between upper and lower separatrices in a pendulum with Hamiltonian $H(x, y) = y^2/2 + \delta \cos(x)$ is $4\sqrt{\delta}$. But we keep the presentation in the scaled version, i.e., with the coefficient of cos equal to 1. The equations are $\dot{x} = y, \dot{y} = \sin(x)$. One can think of a discrete model which, in the limit, behaves as the pendulum. The simplest approach would be to use an explicit Euler method with step $h$, which gives the map $(x, y) \to (x + hy, y + h\sin(x))$. Unfortunately that map is not an APM, but can be made symplectic using a symplectic Euler method: $(x, y) \to (\bar{x}, \bar{y}), \bar{y} = y + h\sin(x), barx = x + h\bar{y}$. If we do not like to have the parameter $h$ in both variables, we simply replace $hy$ by a new variable $z$, rename $z$ again as $y$, introduce $k = h^2$ and we obtain

$$SM_k : \begin{pmatrix} x \\ y \end{pmatrix} \to \begin{pmatrix} \bar{x} = x + \bar{y} \\ \bar{y} = y + k\sin(x) \end{pmatrix}, \tag{10}$$

a popular map known as *standard map* [7]. It is clear that we can look at the variables $(x, y)$ in $\mathbb{S} \times \mathbb{R}$ or

in $\mathbb{T}^2$. It has fixed points located at $(0,0)$, hyperbolic, and at $(\pi,0)$, elliptic, that we denote again as $H$ and $E$. The Figure 8 displays the phase portrait (in $\mathbb{T}^2$) for $k=0.5$ and $k=1$.

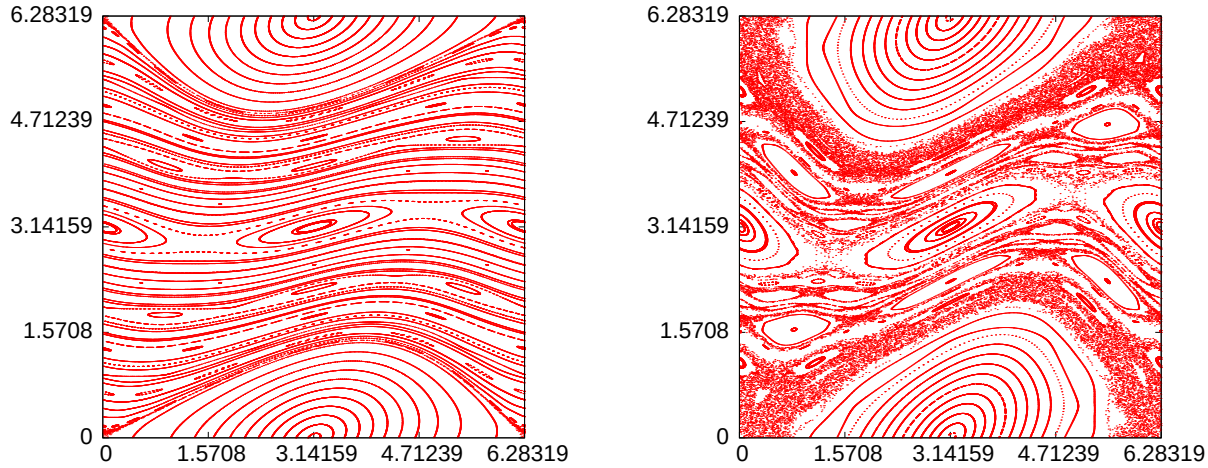


Figure 8: Phase portrait of (10). Left: for $k=0.5$, still quite well ordered. Right: for $k=1$, already with a big amount of chaos. Beyond the main elliptic island around $E$ one can see several islands in both cases. The largest chaotic zone appears around the invariant manifolds of $H$.

On the left plot it is hard to see that the stable and unstable manifolds of $H$ do not coincide. An study like the one in subsection 2.1.2 reveals similar properties. But the strongest difference between these plots is that in the left one there exist rotational IC, that is, IC going from the left vertical boundary to the right one (in this representation; in fact these boundaries are identified). These curves are absent in the right plot. Hence, if we consider the map in $\mathbb{S}\times\mathbb{R}$, there is no obstruction to the dynamics in the $y$ direction. There are points with an initial value $y\in[0,2\pi)$ whose iterates can go arbitrarily far away in the $y$ direction (despite for that value $k=1$ this will require many iterates).

The critical value up to which one has rotational IC is the so-called *Greene's critical value* [18] $k_G\approx 0.971635$. The "last" rotational IC which is destroyed has $\rho=(\sqrt{5}-1)/2$, the golden mean. This is not a surprise. It is the number in $(0,1)$ with best Diophantine properties. The obstruction method using hyperbolic periodic orbits with rotation numbers of the form $F_{n-1}/F_n$ and $F_n/F_{n+1}$, being $F_n$ the $n$-th Fibonacci number, plus a suitable extrapolation, allows to determine $k_G$ accurately. Note also that for $k>k_G$ but close to $k_G$ the rotational IC with $\rho=(\sqrt{5}-1)/2$ is replaced by a Cantor set with "small holes". This supports the claim about the large number of iterates needed to have $y$ far away from the initial location. The *renormalization theory* [26, 27] provides the framework to understand those things in detail.

On the other hand, the Hamiltonian $H(x,y)=y^2/2+\cos(x)$ can be replaced by more complex ones to obtain generalized standard maps. Adding terms in $y^3$ and $y\cos(x)$ allows to explain the asymmetry in Figure 2 right between the inner part and the outer part of the islands and the related inner and outer splittings of the manifolds of the associated periodic hyperbolic points [48]. Replacing $y^2/2$ by $-by+y^3/3$ allows to reproduce a limit flow of the meandering curves, as shown in Figure 4, and other more complex changes give rise to labyrinthine IC with funny shapes [40].

## 2.3 Return maps: the separatrix map

A useful device to understand the dynamics when some hyperbolic invariant object $\mathcal{A}$ has orbits homoclinic to it are the *return maps*. Assume that we have an initial point in a given domain $\mathcal{D}$ close to a point homoclinic to $\mathcal{A}$. Then it approaches $\mathcal{A}$ under iteration, close to $W^s_{\mathcal{A}}$, and after the passage near $\mathcal{A}$ moves away, close to $W^u_{\mathcal{A}}$, and returns to $\mathcal{D}$. Can we describe how the return is produced?

To illustrate with an example we have used a modified Hénon-Heiles potential. In a pioneer example Hénon and Heiles in 1964 used a Hamiltonian with 2 dof (a model of the motion of a star in a galaxy with cylindrical symmetry) [20]. The Hamiltonian they derived is

$$HH(x,y,p_x,p_y)=(x^2+y^2+p_x^2+p_y^2)/2+x^3/3-xy^2, \tag{11}$$

and a careful study of the behaviour of nearby orbits of system (11) lead to the detection of chaotic motion, giving evidence of the lack of integrability, a fact that was proved theoretically later and that was relevant to face integrability problems from an algebraic point of view, see [31] and references therein. Later on the family with Hamiltonian $HH_c(x,y,p_x,p_y) = (x^2+y^2+p_x^2+p_y^2)/2+cx^3-xy^2$ was introduced and the case $c=0$

$$HH_{c=0}(x,y,p_x,p_y) = (x^2+y^2+p_x^2+p_y^2)/2 - xy^2, \tag{12}$$

that we shall use as illustration, presents some interesting particularities. Like many other simple models it has a symmetry wrt to simultaneous change of sign of $y$ and $t$.

One can fix the value of the energy and use $y=0$ as Poincaré section. The Poincaré map $\mathcal{P}$ has a fixed point $H$ which corresponds to a hyperbolic periodic orbit of (12). The invariant manifolds on $HH_{c=0}^{-1}(0.115)$ are shown in Figure 9. There exist homoclinic points and the symmetry implies that the upper branch of $W_H^s$ can be obtained from the lower branch of $W_H^u$.

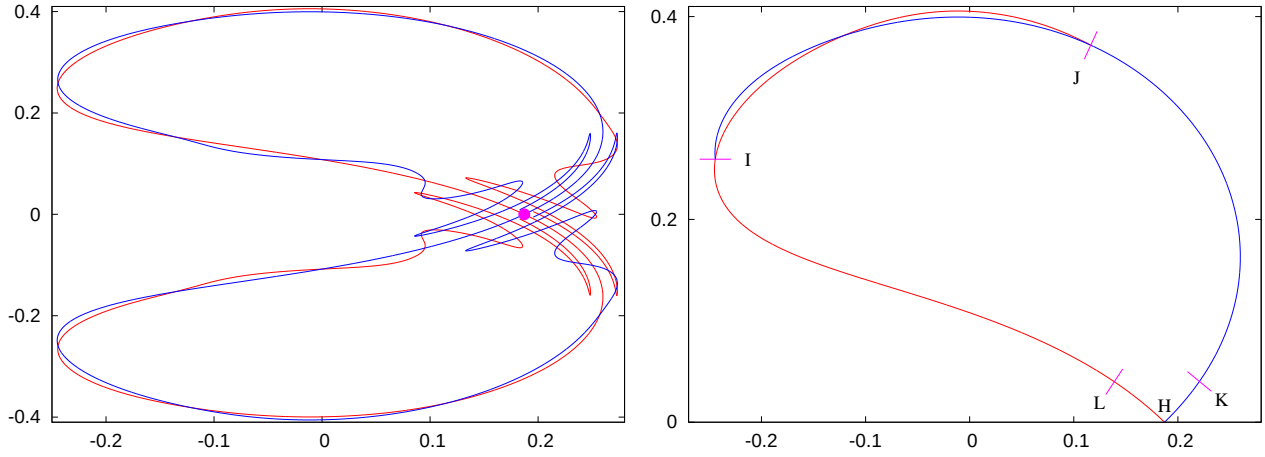


Figure 9: Left: the invariant manifolds ($W^u$ in red, $W^s$ in blue) of the hyperbolic simple periodic orbit of the modified Hénon-Heiles Hamiltonian located inside the domain of admissible conditions on the Poincaré section $y=0$, for the level of energy $h=0.115$. The variables displayed are $(x,p_x)$. Right: a magnification of the upper part showing the location of sections $I,J,K,L$ mentioned in the text. The periodic orbit appears marked as $H$ on the section.

Our goal is to describe the return to a suitable domain $\mathcal{D}$ as a model for a general setting. In Figure 9 right there is a homoclinic point in the segment market as $I$, whose image under $\mathcal{P}$ is the segment market as $J$. A suitable domain can be a strip around the parts of the manifolds between $I$ and $J$. Note that in present case, due to the symmetry, we consider in Figure 9 right only the upper part in the $(x,p_x)$ variables. It can happen that, after passage near $H$, a point moves to the lower part. Hence, it is convenient to consider $\mathcal{D}$ as the union of two strips, symmetric the one from the other, and that we can denote as $\mathcal{D}_+$ and $\mathcal{D}_-$, according to the sign of $p_x$, and define $\mathcal{D} = \mathcal{D}_+ \cup \mathcal{D}_-$.

In general there is no symmetry and then $\mathcal{D}_-$ is not obtained from $\mathcal{D}_+$ by symmetry, and even some of the branches of the manifolds can escape, as it happens for (5).

If we take the part of $W_H^u$ from $H$ to the homoclinic point which appears in $J$, followed by the part of $W_H^s$ between the homoclinic and $H$, and add the symmetric part (on $p_x<0$) we have a *figure-eight pattern* which appears in many problems. This occurs, e.g., for the manifolds of the hyperbolic fixed point of (10). Looking at the map in $\mathbb{S}\times\mathbb{R}$ in suitable coordinates, one has also a figure-eight pattern [49].

First we assume that a point is located in $\mathcal{D}_+$ below $W_H^s$ (the line in blue). After passing close to $H$ it will return to $\mathcal{D}_+$. We follow an elementary method to find the return map. If the splitting is small enough we can assume that the upper branches of the manifolds are coincident and consider a nearby integrable map in the domain bounded by the branches of the manifolds. Let $\varphi_t$ be the flow of a Hamiltonian v.f. with 1 dof in $(x,p_x)$ with Hamiltonian $\mathcal{H}$ such that $\varphi_{2\pi}$ coincides with this integrable map. In particular, points in $I$ move to points in $J$ under $\varphi_{2\pi}$, and we can redefine the strip $\mathcal{D}_+$ as the

set $\cup_{t\in[0,2\pi]}\varphi_t(I)$. The manifolds $W_H^{s,u}$ under that Hamiltonian v.f. coincide and form the separatrix of $\mathcal{H}$. As additional variable in $\mathcal{D}_+$, transversal to that separatrix, we take the level $h$ of $\mathcal{H}$, assuming $\mathcal{H}$ is positive inside the separatrix and equal to zero on it.

For concreteness let us denote as $\lambda$ the dominant eigenvalue of the differential of the map $\varphi_{t=1}$ at $H$. It is clear that the dominant eigenvalue for $\varphi_{t=2\pi}$, close to the one of the initial map, say $\mu$, is $\lambda^{2\pi}$ and that for the Hamiltonian v.f. is $\log(\lambda)$. If $\lambda$ is close to 1 then $\log(\lambda)$ will be close to zero. For simplicity we denote $\log(\lambda)$ as $\lambda^*$. In terms of the dominant eigenvalue of the initial map one has $\lambda^* \approx \log(\mu)/(2\pi)$.

As all the orbits in the domain bounded by the separatrix are periodic, when a point in $\mathcal{D}_+$ returns to it, it has the same value of $h$. But $t$ has changed by the period, which behaves like $c - \log(h)/\lambda^*$, where $c$ is a constant (essentially equal to the time to go from section $L$ to section $K$). The map would be $(t,h) \mapsto (t + c - \log(h)/\lambda^* \,(\mathrm{mod}\ 2\pi), h)$.

Now we return to our original map. The only change is due to the lack of coincidence of $W_H^s$ and $W_H^u$. If we consider the variable $h$ defined as an energy wrt $W_H^u$, when continuing the motion close to $W_H^s$ the energy should be considered wrt that manifold. There is a jump in energy due to the splitting. Note that, using a normal form around $H$ it is possible to define in a natural way an energy in a neighbourhood of this point and to transport that function along both manifolds, by backward or forward iteration, see [10] and also [46] in a general context,. The two energies do not coincide in $\mathcal{D}_+$. The difference is the jump just mentioned. Let us denote it as $s(t)$ (it has a weak dependence on $h$ that we neglect). The simplest expression for $s(t)$ is a sinusoidal oscillation $\varepsilon\sin(t)$ which measures the location of $W_H^u$ wrt $W_H^s$. Then the return map becomes

$$\begin{pmatrix} t \\ h \end{pmatrix} \to \begin{pmatrix} \bar{t} = t + c - \log(\bar{h})/\lambda^* \,(\mathrm{mod}\ 2\pi), \\ \bar{h} = h + \varepsilon\sin(t) \end{pmatrix}. \tag{13}$$

It is clear that the map is not defined if $\bar{h} = 0$ because then the point is in $W_H^s$. On the other hand we have not considered the case $h < 0$. Then the process is similar, but we land on the lower domain $\mathcal{D}_-$. Beyond the variables $(t,h)$ one has to consider a sign $\sigma$ equal to $\pm 1$ in $\mathcal{D}_\pm$. Using also the sign and renaming the variables as $\xi, \eta$, with $\xi \in [0, 2\pi)$ and $\eta$ small, the map (13) becomes

$$SepM : \begin{pmatrix} \xi \\ \eta \\ \sigma \end{pmatrix} \to \begin{pmatrix} \bar{\xi} = \xi + c - \log(|\bar{\eta}|)/\lambda^* \,(\mathrm{mod}\ 2\pi) \\ \bar{\eta} = \eta + \varepsilon\sin(\xi) \\ \bar{\sigma} = \sigma \times \mathrm{sign}(\bar{\eta}) \end{pmatrix}, \tag{14}$$

a map known as *separatrix map*. In a general case the jump $\varepsilon\sin(\xi)$ is replaced by a function $s(\xi)$. In the asymmetric cases one uses different jump functions $s_\pm(\xi)$ according to $\sigma$. The parameter $\varepsilon$, related to the size of the jump or splitting has, typically, exponentially small upper bounds as a function of some physical parameter, like the energy in the case of system (12).

For simplicity we concentrate in the symmetric case and to points passing only through $\mathcal{D}_+$. Then $\sigma = 1$ and we discard it in (14). Now we assume that $\eta$ is close to some fixed value, $\eta_0$, write $\eta = \eta_0 + \zeta$ and $\log(\bar{\eta}) = \log(\eta_0) + \log(1 + \bar{\zeta}/\eta_0) \approx \log(\eta_0) + \bar{\zeta}/\eta_0$, keeping only linear terms in $\bar{\zeta}$. This is a good approximation if $\bar{\zeta}/\eta_0$ is small. If we assume, also, that $\lambda$ is close to 1, then $\lambda^*$ is small. In the $(\xi,\zeta)$ variables the map becomes $(\xi,\zeta) \mapsto (\bar{\xi} = \xi + c_1 + b_1\bar{\zeta},\ \zeta + \varepsilon\sin(\xi))$, where $c_1 = c - \log(\eta_0)/\lambda^*, b_1 = -1/(\eta_0 \times \lambda^*)$ and we do not write explicitly that $\xi$ is taken mod $2\pi$. Finally, define new variables $u = \xi, v = c_1 + b_1\zeta$ and the map becomes

$$\begin{pmatrix} u \\ v \end{pmatrix} \to \begin{pmatrix} \bar{u} = u + \bar{v} \\ \bar{v} = v + b_1\varepsilon\sin(u) \end{pmatrix}. \tag{15}$$

Comparing (15) with (10) we see that they are identical if we set $k = b_1\varepsilon = -\varepsilon/(\eta_0 \times \lambda^*)$. Therefore, we can expect to find invariant curves in the separatrix map at a distance $\eta_0 > \varepsilon/(k_G \times \lambda^*)$ from the location of the invariant manifolds in $\mathcal{D}_+$. A similar reasoning applies in the outer part, when the invariant curves make the full turn around the figure eight. This gives also an estimate of the width of the zone with chaotic dynamics around the split manifolds. The estimate is quite realistic if $\varepsilon$ is very small and $\lambda$ is close to 1. This occurs, for instance, in a case like the Hamiltonian (12) because then, on a level of energy $h$, $\lambda^*$ and $\varepsilon$ are, respectively, of the order of $h$ and exponentially small in $h$.

As final comments in this subsection one has to add that it is very important to derive return maps in higher dimension, like Hamiltonian systems with $\geq 3$ dof or symplectic maps in dimension $\geq 4$. But the formulas that one obtains can be far from simple, due to quasiperiodicity and resonances. To derive, from these return maps, bounds on the distance at which one can find invariant tori, speed of diffusion, etc, is an *open problem*.

# 3 Some theoretical results, their implementation and practical tools

In this section we recall some general results and also provide tools to make them explicit.

## 3.1 A preliminary tool: the integration of the ODE. Taylor method and jet transport

In the case of an analytic Hamiltonian (or general) v.f. like $\dot{x} = f(t,x)$, $x(t_0) = x_0$, $(t_0, x_0) \in \Omega \subset \mathbb{R} \times \mathbb{R}^n$ or $\Omega \subset \mathbb{C} \times \mathbb{C}^n$ one should use integration methods of the initial value problem for ODE. For instance, having in mind to compute Poincaré iterates.

A quite convenient method is *Taylor method*. That is, to obtain the Taylor expansion $x(t_0 + h)$ for suitable values of $h$. If $x(t_0 + h)$ has components $x_i, i = 1, \ldots, n$ we look for a representation

$$x_i = \sum_{s=0}^{N} a_i^{(s)} h^s, \tag{16}$$

for suitable $N, h$, and use it as a one-step method. For further reference we denote as $a^{(s)}$ the vector with components $a_i^{(s)}$.

The point is how to compute the coefficients of the expansion in an easy way to high order.

For a very large class of functions the evaluation of $f$ can be split into simple expressions

$$\begin{aligned}
e_1 &= g_1(t,x), \\
e_2 &= g_2(t,x,e_1), \\
&\vdots \\
e_j &= g_j(t,x,e_1,\ldots,e_{j-1}), \\
&\vdots \\
e_m &= g_m(t,x,e_1,\ldots,e_{m-1}), \\
f_1(t,x) &= e_{k_1}, \\
&\vdots \\
f_n(t,x) &= e_{k_n}.
\end{aligned}$$

Each one of the expressions $e_j$ contains a sum of arguments, a product or quotient of two arguments or an elementary function (like $\sin, \cos, \log, \exp, \sqrt{}, \ldots$) of a single argument. The basic idea is to compute in a recurrent way the power series expansion (up to the required order) of all the $e_j$. The $g_j$ have to be seen as operations with (truncated) power series. Hence we can proceed as follows:

1) Input: $t$ and the components of $x_0$, that is, the coefficients of order zero in (16).

2) Step $s, s \geq 0$: from the arguments of $g_j$ up to order $s$ we obtain the order $s$ terms of $e_j$. In particular for $f_j(t,x)$, which gives the order $s+1$ for $x_j$ (dividing by $s+1$). This is repeated up to the required value of $N$.

3) The values of $N, h$ can be selected so that the truncation error $\sum_{s>N} a_i^{(s)} h^s$ is bounded, for every component, by some small $\varepsilon$ negligible in front of the (unavoidable) round off error.

Under reasonable assumptions, like $c_1\gamma^s \leq ||a^{(s)}|| \leq c_2\gamma^s, 0 < c_1 < c_2$ (which implies radius of convergence $\rho = 1/\gamma$) in the limit when $\varepsilon \to 0$, say $\varepsilon = 10^{-d}$, with $d$ large, one can take $h$ such that the

last term satisfies $||a^{(N)}||h^N = \varepsilon$. It turns out, concerning efficiency, that the optimal value of $h$ tends to $\rho \times \exp(-2)$ (independently of the equation, and where $\rho$ refers to the radius of convergence around the current point $x_0$) and $N \approx d\log(10)/2$ when $\varepsilon \to 0$.

To carry out step 2) above is immediate for the arithmetic operations. As an example for elementary functions we consider the case of powers, that we should use to integrate (1). Let $u(t)=\sum_{s\geq 0} u_s t^s$, $u_0 \neq 0$, $\alpha \in \mathbb{R}$, and we want to compute $v(t) = u(t)^\alpha = \sum_{s\geq 0} v_s t^s$. Then

$$v_0 = u_0^\alpha, \quad v_s = -\frac{1}{su_0}\sum_{k=0}^{s-1} v_k u_{s-k}[k-\alpha(s-k)], \quad \text{for } s>0,$$

the determination being fixed by the one used for $v_0$. This follows easily from $v(t) = u(t)^\alpha$ by taking logarithms and differentiation wrt $t$. Similar recurrences can be obtained for any elementary function. If $f$ contains special functions (e.g., Bessel functions) it is enough to add the ODE satisfied by these functions to the system to be integrated.

To compute to order $N$ has a cost $\mathcal{O}(N^2)$. This is true for the most expensive elementary operations and functions, and it is the basis of the optimal estimates given above, see [22] and slides 1.

In the autonomous case, to obtain the image of a point for a Poincaré map $\mathcal{P}$ through a section $\Sigma$ given by $g(x) = 0$ when $g$ changes from $< 0$ to $> 0$, assume that we have a time $t^*$ such that $g(\varphi_{t^*}(x_0)) < 0$ and $g(\varphi_{t^*+h}(x_0)) > 0$, for the current value of $h$. To find $\mathcal{P}(x_0)$ reduces to solve a 1-dimensional equation, $g(\varphi_{t^*+\delta}(x_0)) = 0$, for the variable $\delta$. This is easily done by using Newton method.

Assume now that we look for a periodic solution. It can be written as a fixed point of a Poincaré map: $G(x_0) = \mathcal{P}(x_0) - x_0 = 0$ for a $x_0 \in \Sigma$. Again this can be solved by Newton method, but this requires to know the differential map $D\mathcal{P}(x_0)$. To this end we integrate, together with the v.f. $f$, the first order variational equations $\dot{A} = Df(\varphi_t(x_0))A$, $A(0) = \mathrm{Id}$. There are two points to take into account, see [37]:

a) The admissible variations of $x_0$ should be confined to the tangent space to $\Sigma$ at that point. Furthermore, if the system has first integrals, like in the Hamiltonian case, this gives additional constrains for $x_0$ and the admissible variations if we fix the levels of these integrals.

b) The return time to $\Sigma$ depends on the initial point. If instead of leaving from $x_0$ we leave from $x_0 + \xi$, being $\xi$ an arbitrarily small admissible variation, the landing time in $\Sigma$ has to be corrected by terms $\mathcal{O}(||\xi||)$. This is relevant to compute $D\mathcal{P}(x_0)$.

In some cases (see subsection 3.4) we can be interested in having an approximation of the Poincaré map not restricted to first order terms in the variations of $x_0 \in \Sigma$, but to higher order: we would like to have the Taylor expansion of $\mathcal{P}(x_0 + \xi)$ to some given order in $\xi$. To this end one can integrate the higher order variational equations, restrict the domain of definition to $\Sigma$ and to the levels of the current first integrals, or proceed in a different, easier, way, using *jet transport* that we describe next.

This can be also applied to obtain the image of a neighbourhood of a point $x_0$ under $\varphi_t$, to see how it depends on parameters (useful to analyze bifurcations), etc.

Assume the initial conditions are $x_0+\xi$, where $\xi$ are some variations and we want to obtain $\varphi_t(x_0+\xi)$ at order $m$ in $\xi$. It is enough to replace all the operations described above to compute $e_j$, in order to obtain the coefficients in (16), done with numbers, by operations with polynomials in $\xi$ up to order $m$. This applies to arithmetic operations, elementary functions, special functions, etc. Hence, instead of the vectors $a^s$ of numerical coefficients in (16) we deal with tables containing the numerical coefficients, up to order $m$, of $n$ polynomials in the $\xi$ variables.

If we return to the case of the Poincaré map, we had to solve $g(\varphi_{t^*+\delta}(x_0)) = 0$, for the variable $\delta$. Now $\delta$ will depend on $\xi$, but this is not a problem for Newton method. We simply apply it replacing numbers by polynomials in $\xi$.

We remark that the jet transport can be implemented in an efficient way. It is also possible to produce rigorous estimates of the tails at every step and to obtain intervals which contain the correct values of all the coefficients. This allows to convert a purely numerical simulation into a Computer Assisted Proof (CAP). See, e.g., [23].

## 3.2 Normal forms

A useful thing, to study many systems, is to try to reduce them to an expression as simple as possible, according to the topics of interest. If we study a discrete map around a fixed point, it would be nice to be able to reduce it to a linear map. In general, this is not possible. Furthermore, we can be interested also on the dependence wrt parameters, to analyze possible bifurcations.

For concreteness we face a Hamiltonian in $n$ dof, in Cartesian coordinates, around a fixed point (located at the origin) that we assume totally elliptic: the eigenvalues are $\exp(\pm \mathrm{i}\,\omega_j), j = 1, \ldots, n$. In canonically conjugate variables $(x_i, y_i), i = 1, \ldots, n$ we write it as $H = \sum_{k\geq 2} H_k$, where $H_k$ denote the homogeneous terms of order $k$ and $H_2 = \sum_{i=1}^n \omega_i (x_i^2 + y_i^2)/2$. In principle, we try to make a change of variables to cancel the terms $H_k, k > 2$. To keep the Hamiltonian character of the v.f. we shall use canonical transformations. These can be easily obtained as the flow of an auxiliary Hamiltonian, $G$, wrt an auxiliary time $s$ until, say, $s = 1$. If you do not want to use a "so big time $s = 1$" simply scale $(x, y) \to \varepsilon(u, v)$, divide the Hamiltonian by $\varepsilon^2$ obtaining $H_2(u, v) + \varepsilon H_3(u, v) + \varepsilon^2 H_4(u, v) + \ldots$ and then the final value of $s$ will be $\varepsilon$. But this is equivalent to the previous approach. What makes the change close to the identity is the smallness of $(x, y)$, not the fact of using $s = 1$.

As we want to cancel, first, the terms in $H_3$, we shall represent $G$ also as a sum of homogeneous parts, starting at order 3: $G = \sum_{k\geq 3} G_k$.

To transform the function $H$ under the change we write $dH/ds = \{H, G\}$, where

$$\{H, G\} = \sum_{i=1}^n \frac{\partial H}{\partial x_i}\frac{\partial G}{\partial y_i} - \frac{\partial H}{\partial y_i}\frac{\partial G}{\partial x_i}$$

denotes the Poisson bracket. Note that the bracket of homogeneous polynomials of degrees $d_1$ and $d_2$ has degree $d_1 + d_2 - 2$. Higher order derivatives are obtained by doing, successively, the Poisson bracket with $G$ once and again. Trying to cancel (if it is possible to cancel) the terms $H_k, k \geq 3$ we determine the homogeneous parts $G_k$. But it turns out that to obtain these parts it is much simpler to use complex coordinates. We introduce

$$\begin{pmatrix} x_i \\ y_i \end{pmatrix} = \frac{1}{\sqrt{2}} \begin{pmatrix} 1 & \mathrm{i} \\ \mathrm{i} & 1 \end{pmatrix} \begin{pmatrix} q_i \\ p_i \end{pmatrix}, \quad i = 1, \ldots, n.$$

Then $H_2$ becomes $\sum_{j=1}^n \mathrm{i}\,\omega_j q_j p_j$.

The transformed Hamiltonian is

$$\varphi_{s=1}^G(H) = H + \{H, G\} + \frac{1}{2!}\{\{H, G\}, G\} + \frac{1}{3!}\{\{\{H, G\}, G\}, G\} + \ldots. \tag{17}$$

Assume we have determined $G_j, j < m$ and we want to cancel all the possible terms to order $m$ in (17). There are terms or order $m$ in (17) which come from $H_m$ or involving $G_j, j < m$, which are already known and that we denote, together, as $K_m$. For definiteness assume $K_m = \sum_{a,b,|a|+|b|=m} K_{a,b}\, q^a p^b$, where $a$ denotes a multiindex with $n$ non-negative components $a_i$, $|a| = \sum_{i=1}^n a_i$ and $q^a = \Pi_{i=1}^n q_i^{a_i}$, as usual. Similar for $b$ and $p^b$. The only unknown part comes from $G_m$, that we also write as $G_m = \sum_{a,b,|a|+|b|=m} G_{a,b}\, q^a p^b$ and we would like to have

$$0 = \{H_2, G_m\} + K_m = \sum_{a,b,|a|+|b|=m} \mathrm{i}\,(\omega, b - a) G_{a,b}\, q^a p^b + \sum_{a,b,|a|+|b|=m} K_{a,b}\, q^a p^b, \tag{18}$$

where $(\omega, b - a)$ denotes the scalar product $\sum_{j=1}^n \omega_j (b_j - a_j)$. As $K_{a,b}$ is known, one determines easily $G_{a,b}$, provided $(\omega, b - a) \neq 0$. But it is clear that if $b_j = a_j$ for all $j$, then the term $K_{a,a}$ must be left on the transformed Hamiltonian, independently of $\omega$. These are called the *unavoidable resonances* which appear at even orders. Furthermore, if $\omega$ is *resonant*, i.e., there are integers $c_j, j = 1, \ldots, n$, such that $(\omega, c) = 0$, other terms should be kept in the transformed Hamiltonian when $b - a = c$. These are the additional resonant terms.

The normalization process can be continued to any order. But, in general, unless the Hamiltonian is integrable, the formal normal form is not convergent. One can expect that it belongs to some Gevrey class (see subsection 2.1.2), but I am not aware of *concrete general results* in that direction.

After we have transformed the Hamiltonian up to order $M$, we can skip the terms of higher order and denote the contribution up to order $M$ as $HNF_M$, the *normal form to order* $M$. We recall that a Hamiltonian system with $n$ dof is said to be *integrable* (in the Liouville-Arnold sense) if there exist $n$ first integrals, $F_j, j = 1, \ldots, n$, in involution, $\{F_i, F_j\} = 0$, and functionally independent almost everywhere. If $\omega$ is non-resonant then the $HNF_M$ is integrable, because one can take $F_j = q_j p_j, \forall j$.

Now consider the resonant case. It is clear that, by construction, $\{H_2, HNF_M\} = 0$ and, therefore, except in the degenerate case in which they are not independent, if $n = 2$ one has $HNF_M$ integrable. In general this is not true if $n > 2$. The system can be far from integrable even in a small vicinity of a totally elliptic point. But it can take a long time to have numerical evidence of the existence of chaos, even if it occurs for most of the initial conditions.

A celebrated theorem by Arnold says that, for an integrable system, if the set of points in the phase space corresponding to fixed values of the first integrals $F_1^{-1}(c_1) \cup F_2^{-1}(c_2) \cup \ldots \cup F_n^{-1}(c_n)$ is compact, then it is an $n$-dimensional torus $\mathbb{T}^n$. Around a given torus one can introduce the so-called *action-angle variables* $(I, \varphi), I \in \mathbb{R}^n, \varphi \in \mathbb{T}^n$. The integrable system can be written, then, as depending only on $I$: $H = H_0(I)$, the integration is elementary and the frequencies on the given torus have the expression $\omega_j = \partial H_0 / \partial I_j|_{F=c}, j = 1, \ldots, n$. If the system is perturbed to $H = H_0(I) + \varepsilon H_1(I, \varphi)$ we can study how the properties of $H_0(I)$ change under the effect of the perturbation. See subsections 3.3 and 3.5 in this direction.

But we want to point out that it is also possible to try to produce a normal form for the perturbed Hamiltonian around the given torus if the frequencies on it, $\omega_j$ satisfy a non-resonant condition. This can push the perturbation to higher order in $\varepsilon$, making easier the applicability of general results.

Up to now we have considered, around a fixed point, the totally elliptic case. If the quadratic term $H_2$ contain some hyperbolic part $H_2 = \sum_{i=1}^{n_e} \omega_i (x_i^2 + y_i^2)/2 + \sum_{j=n_e+1}^{n} \lambda_j x_j y_j$, one can use similar ideas to obtain approximations of the central manifold and of the Hamiltonian reduced to it. We return to this in subsection 3.4.

## 3.3 Stability results: KAM theory and related topics

There is a natural generalization of the idea of twist map to higher dimension. Consider a map $T$ defined, in suitable coordinates, in a product of $n$ annuli, with radii $r_i \in (r_{d,i}, r_{u,i}), 0 < r_{d,i} < r_{u,i}$, $i = 1, \ldots, n$, of the form $T(r, \alpha) = (r, \alpha + a(r))$, where $r \in \mathcal{R} = \Pi_{i=1}^n (r_{d,i}, r_{u,i})$ has components $r_1, \ldots, r_n$, $\alpha \in \mathbb{T}^n$ and $a$ is a map from $\mathcal{R}$ to $\mathbb{R}^n$ which can be denoted as *translation*. The map $T$ is an integrable symplectic map and $\mathcal{R} \times \mathbb{T}^n$ is foliated by tori invariant under $T$. Nothing else that what we saw for (7) in subsection 2.1.1.

The differential of the translation with respect to the radii, $D_r a(r)$ is know as *torsion*.

Then the KAM theorem for symplectic maps has the following statement, completely analogous to Theorem 2.1.

**Theorem 3.1.** *Consider a perturbation $F_\varepsilon = T + \varepsilon P$ of the integrable symplectic map $T$ in $\mathcal{R} \times \mathbb{T}^n$ and assume that for $r = r^*$ the vector $a(r^*)$ satisfies a DC, that the torsion is non-degenerate and $\varepsilon$ is small enough. Then the map $F_\varepsilon$ has also invariant tori in $\mathbb{T}^n$, close to $r = r^*$, and on them the action of $F_\varepsilon$ is conjugated to the one of $T$ on $r = r^*$, that is, a translation by $a(r^*)$.*

In present case the DC is slightly different from the one in (3). Beyond the translations $a_i(r), i = 1, \ldots, n$, one has to add the value 1, as it is obvious thinking on the suspension. So, it reads as

$$|(\sum_{i=1}^{n} k_i, a_i) + k_0| \geq b|k|^{-\tau}, \quad \forall k \in \mathbb{Z}^{n+1} \setminus \{0\},$$

where $k$ denotes now $(k_1, \ldots, k_n, k_0)$. The role of the DC, the non-degeneracy of the torsion, analogous to the twist condition, and the smallness of $\varepsilon$ play the same role.

A result similar to Theorem 3.1 holds in the case of Hamiltonian systems.

**Theorem 3.2.** *Let $H_0(I)$ be an integrable Hamiltonian, for which there exist invariant tori, and assume that for some given torus, labelled by $I^*$, the frequencies $\omega(I^*) = \partial H_0(I)/\partial I|_{I=I^*}$ satisfy a DC (in the sense of (3)) and are non-degenerate, so that the differential $\partial\omega/\partial I|_{I=I^*}$ is regular. Then if $\varepsilon$ is small enough, a perturbed Hamiltonian $H(I,\varphi) = H_0(I) + \varepsilon H_1(I,\varphi,\varepsilon)$ has a nearby invariant torus with the same frequencies.*

These results usually do not give estimates on how small $\varepsilon$ should be or, if any, they are very pessimistic. However, normal form techniques, see subsection 3.2 can help to start the iterative process in a very good approximation, so that the difference with the initial guess and the true torus, if it exists, is sufficiently small.

For the effective computation of invariant tori there exist different methods.

A quite classical method is the Lindstedt-Poincaré (LP) method. In principle it is formal because one looks for the invariant tori without paying too much attention to the DC (despite this can also be implemented). Assume that we look for 2D tori around a totally elliptic point (assumed to be located at the origin) in a Hamiltonian system with $n = 2$ dof. Let $\omega_1(0), \omega_2(0)$ be the frequencies at the fixed point. The linear system will have, for the $q, p$ variables, a representation as linear combinations of $\cos(\omega_1(0)t + \psi_1), \cos(\omega_2(0)t + \psi_2)$, where $\psi_1, \psi_2$ represent some phases, and these terms have amplitudes $\alpha_1, \alpha_2$. Due to symmetries and the freedom to select the origin of time the phases for the different variables can be put in simple form.

We ask to satisfy the equations $\dot{q} = \partial H/\partial p, \dot{p} = -\partial H/\partial q$ by expanding in powers of the amplitudes $\alpha_1, \alpha_2$ and integration of the coefficients of these powers with respect to time. However, it turns out that at some order we can find on the right-hand side of the equations terms which are not purely quasiperiodic, i.e., they are constant. The solution consists in allowing the frequencies to depend also on the amplitudes. So $\omega_i = \omega_i(0) + \sum_{j_1,j_2} c_{i,j_1,j_2}\alpha_1^{j_1}\alpha_2^{j_2}$, $i = 1, 2$, and a suitable choice of these $c_{i,j_1,j_2}$ coefficients cancels the constant terms.

A quite used method is based in writing the coordinates of the points of the unknown torus as Fourier series in some angles and impose the invariance conditions. For concreteness we consider the case of symplectic maps. The flow case can be reduced to this one via a Poincaré map. Assume that we look for a $d$-dimensional torus in which the dynamics is conjugated to $\theta \mapsto \theta + \alpha$ for $\theta \in \mathbb{T}^d$ and a translation vector $\alpha \in \mathbb{R}^d$ satisfying the DC. Let $x$ be the coordinates in the phase space and $F$ the discrete map. The invariance condition is

$$F(x(\theta)) = x(\theta + \alpha). \tag{19}$$

It is clear that one has freedom to select the origin of the angles $\theta_i$ and that eventual symmetries can reduce the number of coefficient the be determined.

To begin with the process, we can assume that we have obtained some approximation by direct numerical simulation, or that we start near a fixed (or periodic) point and use the linear approximation or an approximation obtained by LP method. If we are interested in a family of invariant tori, one can use continuation methods, but taking into account that the values of $\alpha$ should satisfy the DC. Hence, there will be gaps in the family, despite they can be very small in some cases. Let $c$ denote, generically, the coefficients of the Fourier expansion, truncated at a suitable order. From a grid of values of $\theta$ one can obtain initial values of $x$. They are mapped to $F(x)$ and the images can be Fourier analyzed to obtain the new Fourier coefficients $\hat{c}$. Let $L$ be the action of the translation by $\alpha$ on the initial Fourier coefficients. According to (19) we should require $L(c) - \hat{c} = 0$. This is the equation that follows from (19) and has to be solved, usually by Newton method. The differentials of the Fourier synthesis and analysis are elementary and the one of $F$ can be obtained by computing $DF$ (this can be, typically, the differential of a Poincaré map). See [21] for an efficient implementation with similar and extended ideas, which works even with a very large number of harmonics.

The number of harmonics to be used depends on the shape of the torus. One can use in the grid in $\theta$ (and, therefore, in $x$) a number of points larger than the number of components of $c$. In that way one can check the behaviour of coefficients in $\hat{c}$ which have not been used as $c$ coefficients in the representation

of the solution we search, and see if they can be neglected. Otherwise one increases the number of harmonics. This can be done at successive iterations of Newton method in a dynamic way.

It is also possible not to fix $\alpha$ a priori and determine it together with the coefficients $c$. Note that in case $\alpha$ is close to resonant, one can have convergence problems. For other quite different problems, like looking for invariant tori in PDE, this method requires a huge number of Fourier coefficients if the discretisation dimension is large. Other methods, working directly in the phase space, like the synthesis of a return map, see [39, 36] can give the desired results.

There is a fact, concerning invariant tori, and which applies also to the computation of some periodic orbits, which can produce difficulties. This is the instability present in partially normally hyperbolic tori or, in a simpler case, in linearly unstable periodic orbits. Given a point $x$, and assuming it approximately located in an invariant torus, the instability can produce that $F(x)$ is far away from the torus. This produces convergence problems.

The solution consist in using *parallel shooting*. Instead of taking a single Poincaré section, say $\Sigma$, one can use several of them: $\Sigma_0 = \Sigma, \Sigma_1, \Sigma_2, \dots \Sigma_{m-1}$ and the corresponding *partial Poincaré maps*: $\mathcal{P}_1 : \Sigma_0 \mapsto \Sigma_1,\ \mathcal{P}_2 : \Sigma_1 \mapsto \Sigma_2, \dots, \mathcal{P}_m : \Sigma_{m-1} \mapsto \Sigma_0$. Hence, the full Poincaré map can be written as $\mathcal{P} = \mathcal{P}_m \circ \dots \mathcal{P}_2 \circ \mathcal{P}_1$. Then we look for Fourier representations in each one of the intermediate sections. This produces a much large set of equations but it has the advantage that each one of the partial maps $\mathcal{P}_j$ is much less unstable.

In the case of highly unstable periodic orbits the things are simpler. We only need one point in each intermediate section, say $x_0 \in \Sigma_0, x_1 \in \Sigma_1, \dots, x_{m-1} \in \Sigma_{m-1}$. The conditions are simply $\mathcal{P}_1(x_0) - x_1 = 0, \mathcal{P}_2(x_1) - x_2 = 0, \dots, \mathcal{P}_m(x_{m-1}) - x_0 = 0$. The system to be solved is large but the differential has a simple block structure and the condition number is much better.

## 3.4 Invariant manifolds

Another basic ingredient of the dynamics are the invariant manifolds. In contrast with the tori of maximal dimension, responsible of the regular behaviour, the invariant manifolds are, typically, responsible of the chaotic part of the dynamics. We comment first on invariant stable and unstable manifolds of fixed points of APM $F$. The components will be denoted as $F_1, F_2$.

Assume a fixed point is located at the origin with dominant eigenvalue $\lambda > 1$ and having an unstable linear subspace $E^u$ and a stable one $E^s$. Then the *unstable manifold Theorem* ensures the existence of an unstable manifold $W^u_{\text{loc}}$ in a neighborhood of the origin, invariant under $F$, tangent to $E^u$ at the origin and such that for a point $p$ on it, the iterates under $F^{-1}$ tend to the origin. In fact, only the points in $W^u_{\text{loc}}$ remain on the neighborhood for all iterations. This is a local result. Then the global unstable manifold $W^u$ is obtained by iteration of $W^u_{\text{loc}}$ under $F$. A similar result gives the stable manifold, obtained by exchanging $F$ and $F^{-1}$. In the analytic case, as we assume, the manifolds are analytic.

Let $u$ and $s$ be local coordinates along the unstable and stable eigenvectors. For the linear map $DF$ the manifold $W^u$ is just $s = 0$. We can try to find a representation of $W^u$ for $F$ as the *graph of a function*: $s = g(u) = \sum_{j\geq 2} a_j u^j$. The invariance condition reads $F_2(u, g(u)) = g(F_1(u, g(u)))$. The coefficients $a_j$ are determined in a recurrent way by identifying the left and right coefficients of $u^j$.

An alternative representation of $W^u$ is the *parametrization method*. Let us use $z$ as a parameter. In the linear case a point with $u = z$ is mapped to $u = \lambda z$. Now it is not necessary to use coordinates adapted to the eigenspaces. If we use $(x, y)$ as coordinates around the fixed point and represent the parametrization as $(p_1(z), p_2(z))$, the invariance condition is simply

$$F(p_1(z), p_2(z)) = (p_1(\lambda z), p_2(\lambda z)). \tag{20}$$

That is, we look for a conjugacy on the manifold between $F$ and its linear part. We search now for the parametrization as $p_1(z) = \sum_{j\geq 2} a_j z^j$, $p_2(z) = \sum_{j\geq 2} b_j z^j$ in (20). Note that the parametrization can be normalized so that the vector of coefficients of order 1 has Euclidean norm equal to 1. As before, the coefficients of order $j > 1$ are obtained in a recurrent way. This is the method used for many of the examples displayed before.

A first practical question, given a parametrization to order $N$ (a similar question can be posed for the graph method), is up to which value of $z$, say $z_{\max}$ one can use the representation. The idea is quite simple: given a tolerance $\varepsilon$ we can compute the point $B$ of parameter $z$ and also the point $A$ of parameter $z/\lambda$. One should have $F(A) = B$, according to (20). Hence, we can check up to which value of $z$ one has $||F(A) - B|| < \varepsilon$. This gives the admissible domain for $z$. Then, a *fundamental domain* $\mathcal{FD}$ is parametrized by $z \in (z_{\max}/\lambda, z_{\max}]$. Any point on the manifold can be found as an iterate of a point in $\mathcal{FD}$. A similar domain, with $z < 0$, has to be found for the other branch of the manifold.

To obtain points in the manifold for $z > z_{\max}$ we simply divide the current parameter by $\lambda$ as many time as required until a value less than $z_{\max}$ is obtained. Assume one has to divide $k$ times. Then we compute the point of parameter $z/\lambda^k$ and iterate it $k$ times under $F$. In this way it is possible to reach points away from the fixed one, to detect foldings of the manifold, to reach the vicinity of a homoclinic or heteroclinic point, etc. The selected values of $z$ at which the computation is done can be chosen to satisfy conditions like to have the distance between two consecutive points in $W^u$ or the angle between three consecutive points below some prefixed values.

Why to use approximations beyond the linear one? The answer depends on the purpose. If we want to produce a long part of the manifold and, specially, if $\lambda$ is close to 1, one can required many iterates. On the other hand, if $F$ is not given explicitly but follows from a Poincaré map, one needs jet transport to have a local Taylor expansion. In any case, there is an optimal choice to obtain the "cheaper order" (cheaper can mean in terms of CPU time, of personal time, or a combination of both).

If we are interested in locating an homoclinic point, and no symmetry is available for this, the problem reduces to find two parameters, $z_u$ and $z_s$, and well as two integers, $k_u$ and $k_s$, to be used for the unstable and stable manifolds, respectively, such that $F^{k_u}(p_u(z_u)) = F^{-k_s}(p_s(z_s))$ where $p_u, p_s$ denote the respective parametrizations. It is possible to find suitable values of $k_u, k_s$ and then to solve for $z_u, z_s$ using Newton method. A similar method can be used for heteroclinic points, for tangencies, etc.

The ideas are similar in higher dimension. One can look for $d$-dimensional invariant manifolds, $d > 1$, using either graph or parametric methods. This is specially necessary, for instance, if we look for an unstable manifold with quite different eigenvalues. A low order representation will take the initial points along the direction of the maximal eigenvalue. Beyond using high order local expansions, to decrease the problem, one can use different devices depending on the problem.

To look for the invariant unstable manifold of an invariant curve in a symplectic 4D map, a parametrization using a parameter $z$, which measures the distance to the curve, and an angle $\theta$ along the curve are useful. The fundamental domain, in that case, is diffeomorphic to an annulus. See an example in subsection 4.2 in a different context and another one in subsection 4.5 concerning a family of invariant curves.

The idea extends to any dimension with increasing complexity. See [2, 3, 4] for a nice global approach.

A different problem appears when we consider symplectic maps in dimension 4 (or higher) or problems reducible to them. Consider again the case of a fixed point but assume that, together with an eigenvalue $\lambda > 1$ and its inverse, there is a couple of eigenvalues of modulus 1. They give rise to the *centre manifold* of the point. In general, when we consider a given neighborhood of the point, the manifold has some degree of differentiability which depends on the neighborhood. Furthermore, there is no uniqueness in general.

The difficulty comes from the fact that the dynamics on that manifold is not known. It can contain, simultaneously, invariant curves, periodic points and chaotic zones. It is said to be a *normally hyperbolic invariant manifold* (NHIM) if the hyperbolicity normal to the manifold is stronger than the hyperbolicity that can be found inside the manifold.

One can recur to normal forms to obtain an approximation of all the dynamics around the point and, in particular, the centre manifold. A similar idea is to use a *partial normal form*, see [39]. Assume we have a Hamiltonian

$$H = \lambda q_1 p_1 + \frac{1}{2}\omega_1(q_2^2 + p_2^2) + \frac{1}{2}\omega_2(q_3^2 + p_3^2) + \sum_{k\geq 3} H_k(q_1, q_2, q_3, p_1, p_2, p_3), \tag{21}$$

where, as usual, $H_k$ denotes a homogeneous polynomial of degree $k$.

We proceed as in the case of normal form above, but trying only to cancel all the terms such that the total degree in $(q_1, p_1)$ is equal to 1. Using again complexification, as in the case of the normal form, for the couples $(q_2, p_2)$ and $(q_3, p_3)$, the current denominators to obtain the successive terms in the Hamiltonian $G$ used to transform $H$ are of the form

$$(k_1 - l_1)\lambda + \mathrm{i}\,(k_2 - l_2)\omega_1 + \mathrm{i}\,(k_3 - l_3)\omega_2,$$

with modulus bounded from below by $|\lambda|$, even if $\omega_1$ and $\omega_2$ are resonant. It is clear that, denoting the new variables as $Q_1, Q_2, Q_3, P_1, P_2, P_3$, if we set $Q_1 = P_1 = 0$ this is the desired centre manifold. Hence, setting these variables to zero we have a Hamiltonian with 2 dof, which gives the reduction to the centre manifold of the initial Hamiltonian. The process is formal, there is no convergence in general, but one can obtain a good approximation in a suitable domain. One can check up to which distance of the fixed point the approximation satisfies some tolerance condition. See [39] for an example around the collinear point $L_2$ in the spatial circular restricted three body problem.

## 3.5 Instability, bounds and detection

In the case of a Hamiltonian with $n \geq 3$ dof, in principle, there is no way to avoid diffusion. The maximal dimensional tori have dimension $n$, that is, codimension $n-1$ in a fixed level of energy, and they do not separate the phase space. For instance, initial conditions as close as we like to $L_{4,5}$ in the spatial circular restricted three-body problem, see beginning of section 4, which are totally elliptic fixed points, can go far away from these points. But normal forms, or averaging, lead to the so-called Nekhorosev estimates [34], showing that one needs an extremely large time if one starts close enough to the libration point. Similar things happen for $(2n-2)$-dimensional symplectic maps.

Consider a perturbation $H(I, \varphi) = H_0(I) + \varepsilon H_1(I, \varphi, \varepsilon)$ of an integrable Hamiltonian $H_0$. The basic idea of the bounds is similar to the averaging Theorem 1.1, trying to cancel, around an arbitrary torus labelled by the action $I^*$, the dependence wrt $\varphi$. But now the frequencies of the unperturbed Hamiltonian $\omega(I) = DH_0$ maybe do not satisfy the DC and, on the other hand, the perturbation will produce that the frequencies change. Hence, the passage through resonances or through other frequencies not satisfying the DC is unavoidable.

First one should examine which is the effect of a resonance. We refer to subsection 2.2 where we commented on the width associated to a pendulum like structure. A perturbation $\mathcal{O}(\varepsilon)$ can give rise to variations $\mathcal{O}(\sqrt{\varepsilon})$ due to the presence of a simple resonance. This happens if the frequencies change, reach a resonance and they go away from it. But then one can put the following question. Assume that in the variation of some action there is a term, due to the perturbation, like $\dot{I}_j = \varepsilon \cos((k, \varphi))$, where $(k, \varphi)$ is a linear combination of the angles, and the related combination of the frequencies satisfies $(k, \omega) = 0$. One expects that the frequencies will change with time and one will escape from resonance, but it can happen that the *frequencies are locked at resonance up to order* $m$ for some $m > 0$. That is, $\frac{d^k}{dt^k}(k, \omega) = 0$ for $k = 0, 1, \ldots, m$, $\frac{d^{m+1}}{dt^{m+1}}(k, \omega) \neq 0$. Then, during a long time the term $\cos((k, \varphi))$ will be close to constant and the action can change by a large amount. If the locking occurs at all orders the change in $I_j$ will be $\mathcal{O}(\varepsilon t)$. To prevent this locking is why Nekhorosev introduced the so-called *steepness condition* which prevents that the order of the locking exceeds a maximal value. Then one has the Nekhorosev result: Under steepness of some order the variation of the actions $||I(t) - I(0)||$ do not exceeds a bound $\mathcal{O}(\varepsilon^b)$ during a time interval $|t| < \mathcal{O}(\exp(c\varepsilon^{-a}))$, where the positive constants $a, b, c$ depend on the order of steepness and properties of $H_0$, assuming that the norm of $H_1$ is bounded.

Around a given point, or a given torus (in particular, a periodic orbit) it can happen that there are many KAM tori. The above description of the Nekhorosev estimates puts a bound on how fast can be the escape from the vicinity of these tori. Typically one refers to this fact as *stickiness of the invariant tori*. Perhaps the escape is so slow that has no relevance during the time interval in which we are interested, or even during the period of validity of the model. This suggests to introduce the concept of *practical stability*. Assume that the studied object has $I = I^*$. Then, for fixed values of $(\varepsilon, T)$, where $\varepsilon$ is moderately small and $T$ is large, we say that there is $(\varepsilon, T)$-practical stability if there exists $\rho = \rho(\varepsilon, T)$,

such that points with initial conditions at $t = 0$ satisfying $||I(0) - I^*|| < \rho$ evolve with time satisfying $||I(t) - I^*|| < \varepsilon$ for all $t \in [0, T]$. That is, we require stability only for finite time.

Clearly, for any v.f. with Lipschitz constant $L$, $(\varepsilon, T)$-practical stability is found if $\rho \leq \varepsilon \exp(-LT)$, as follows from Gronwall lemma. But this gives *extremely small* values of $\rho$, completely useless for any practical application. More realistic values would be $\rho = 0.01$ for $\varepsilon = 0.02$ and $T = 10^9$, depending on the practical example in mind.

See, e.g., [9] for a nice approach to KAM and practical stability simultaneously.

Another relevant point is how to detect the existence of chaos and quantify it in a concrete example. There are many different approaches. We comment on the Lyapunov exponents.

To measure the instability properties of a fixed point (of a continuous or discrete system) it is enough to look at the differential of the v.f. or of the map at that point. How to proceed for a general orbit? The idea is to look for the rate of increase (if any) of the distance between the orbits of nearby points. In the limit, this becomes the rate of increase of an initial displacement, $\xi$, under the differential of the iterates of the map or under the action of the first order variational flow. For concreteness we consider the case of discrete maps.

Let $x_0$ be an initial point on a manifold $\mathcal{M}$ on which it acts a map $F$ and let $x_1 = F(x_0), \ldots, x_k = F(x_{k-1}), \ldots$ the orbit of $x_0$. We can define, if it exists,

$$\Lambda = \sup_{\xi} \lim_{k \to \infty} \frac{\log(||DF^k(x_0)\xi||)}{k}, \tag{22}$$

where $\xi$ is taken from the vectors with unit norm $||\xi|| = 1$ in the tangent space to $\mathcal{M}$ at the point $x_0$: $T_{x_0}\mathcal{M}$. One can prove that the limit in (22) exists for almost every $x_0 \in \mathcal{M}$ and for almost every $\xi \in T_{x_0}\mathcal{M}$, and it is known as *maximal Lyapunov exponent*.

In the Hamiltonian case (or in the symplectic one), it is easy to prove that for initial points in invariant tori of maximal dimension the limit exists and is equal to zero. Typically $||DF^k(x_0)\xi||$ behaves linearly in $k$ in that case, which gives the desired limit. For generic unstable orbits one expects positive values of $\Lambda$. The geometrical reason is clear: every time that the iterates pass close to an hyperbolic object, the unstable component will increase at a geometric rate. For an integrable system, if, for instance, unstable and stable manifolds coincide, when returning near the hyperbolic object, this expansion is canceled due to the iterations which occur close to the stable manifold. But the existence of transversal homoclinic (or heteroclinic points) prevents this to occur.

One of the basic questions is how to have an estimate of the limit. In practice the number of iterations should be finite (and there is also the effect of round off, which is another issue). A simple approach is to proceed to the computation in (22) using a different presentation. Let us define the *Lyapunov sums* as follows: Let $x_0, \xi_0$ be the initial point and vector and set $S_0 = 0$. Then, at the $k$th iterate, we use the following algorithm:

$$x_k = F(x_{k-1}), \quad \eta_k = DF(x_{k-1})\xi_{k-1}, \quad \xi_k = \eta_k/||\eta_k||, \quad S_k = S_{k-1} + \log(||\eta_k||). \tag{23}$$

Hence, we normalize the tangent vector after every step and add the log of the normalization to the current value of the sum $S$. It is clear that the limit slope of $S_k$, as function of $k$, should coincide with $\Lambda$, as defined in (22). Hence, we can proceed as in (23) and, from time to time (say, after $mN$ iterates, $m = 1, 2, \ldots$), fit a line to three different subsamples of the current sample (e.g. last 30%, last 50% and last 70%) and accept the average of the slopes as value of $\Lambda$ if they differ by less than a prescribed tolerance. Otherwise, keep doing iterates until the next multiple of $N$, provided this do not exceeds a maximal value.

A problem is that, in case $\Lambda = 0$, the convergence can is slow. For instance, $\log(k)/k$ is below $10^{-5}$ only for $k \geq 1,416,361$. An alternative approach, which tends in a faster way to the limit and also smoothes out the oscillations due to the quasiperiodic effects (in the case of orbits) can be found in [8]. One can look for the systematic use of that method in [24] for a family of 2D symplectic maps in $\mathbb{S}^2$. Another idea, if one is interested only in deciding whether the orbit is regular or chaotic, is to stop computations and consider the orbit as chaotic if $S_k$ exceeds some threshold.

# 4 Applications to Celestial Mechanics

In this section we present several applications to illustrate theoretical and computational approaches to simple examples in Celestial Mechanics. One can have a look at slides 3. concerning the role of dynamical systems in celestial mechanics. Most of the applications deal with the Restricted Three-Body Problem (RTBP). We shortly recall it.

The RTBP studies the motion of a particle $P_3$ of negligible mass under the gravitational attraction of two massive bodies, $P_1$ and $P_2$, of masses $m_1$ and $m_2$, respectively. They are known as primaries or as primary and secondary. We assume that the primaries move in a plane along circular orbits around their centre of masses. We can normalize $m_1 + m_2 = 1$ and $d(P_1, P_2) = 1$ and express the dynamics in a rotating frame (the so-called synodical frame) with unit angular velocity. The problem depends on a unique parameter $\mu = m_2$. In this frame $P_1$ and $P_2$ are kept fixed at $(\mu, 0, 0)$ and $(\mu - 1, 0, 0)$.

The equations of motion are

$$\ddot{x} - 2\dot{y} = \Omega_x, \quad \ddot{y} + 2\dot{x} = \Omega_y, \quad \ddot{z} = \Omega_z, \tag{24}$$

where $\Omega(x, y, z) = \frac{1}{2}(x^2+y^2)+\frac{1-\mu}{r_1}+\frac{\mu}{r_2}+\frac{\mu(1-\mu)}{2}$, being $r_1^2 = (x-\mu)^2+y^2+z^2$, $r_2^2 = (x+1-\mu)^2+y^2+z^2$. The function $J(x, y, z, \dot{x}, \dot{y}, \dot{z}) = 2\Omega(x, y, z) - (\dot{x}^2 + \dot{y}^2 + \dot{z}^2)$ is a first integral, its value being known as Jacobi constant and it is usually represented as $C$. The related 5D energy manifolds are defined as

$$\mathcal{M}(\mu, C) = \left\{(x, y, z, \dot{x}, \dot{y}, \dot{z}) \in \mathbb{R}^6 | J(x, y, z, \dot{x}, \dot{y}, \dot{z}) = C\right\} \tag{25}$$

and their projections on the configuration space are known as Hill's regions, bounded by the zero velocity surfaces (ZVS) (the zero velocity curves, ZVC, in the planar case).

The problem has five equilibrium points (also known as libration points):

- Three of them collinear (or Eulerian) on the $x$ axis, $L_{1,2,3}$, of centre×centre×saddle type and, hence, they have a 4D centre manifold which contains the so-called horizontal and vertical periodic orbits of Lyapunov type (to be denoted as $\text{hpo}_L$ and $\text{vpo}_L$), invariant 2D tori and other periodic orbits (like the halo orbits, depending on the value of $C$), as well as chaotic regions.
- Two of them triangular (or Lagrangian), $L_{4,5}$, at $x = \mu - 1/2$, $y = \pm\sqrt{3}/2$, $z = 0$. The term $\mu(1-\mu)/2$ in $\Omega$ is added to have $C(L_{4,5}) = 3$. Let $\mu_j$ be the value of $\mu$ for which the ratio of frequencies in the plane, $\left[(1 \pm (1 - 27\mu(1-\mu))^{1/2})/2\right]^{1/2}$ is $j$. The points are totally elliptic for $0 < \mu < \mu_1 = (9 - \sqrt{69})/18$ and the 2:1, 3:1 resonances (leading to instability) show up for $\mu_2 = (45 - \sqrt{1833})/90$ and $\mu_3 = (15 - \sqrt{213})/30$. Associated to the planar frequencies there are the so-called short and long period periodic orbits. The vertical frequency, giving rise also to a family of $\text{vpo}_L$, is equal to 1.

## 4.1 An elementary mission around $L_1$

First we consider the planar case. Assume that $P_1$ and $P_2$ are Sun and Earth, respectively. The distance between them and the period ($1.5 \times 10^8$ km, 1 year) are scaled to 1 and $2\pi$ units as said before and we take $\mu = 3.0404326 \times 10^{-6}$ (it includes Moon's mass). We want to carry out the following steps:

i) Compute a periodic orbit of the system, around the Earth, with a period of 1 day (a geostationary orbit) and check that it is close to circular. Call it $\text{PO}_1$.

ii) Compute some periodic orbits around $\text{L}_1$ (of the $\text{hpo}_L$ family), which are symmetrical wrt the $x$ axis. Check that they are unstable. We call them, in general, $\text{PO}_2$.

iii) Compute the left branches of the stable manifolds of the previous orbits until they reach some suitable value of $x$ (e.g., $x = -0.999$).

iv) Now assume an spacecraft is moving in the "parking" orbit $\text{PO}_1$. At some point of the orbit we give an impulsion $\Delta v$, in the direction of the velocity at that point, with the goal of reaching a point of the stable manifold of one of the $\text{hpo}_L$. Determine the $\text{hpo}_L$ which are reachable in that way from the parking orbit, at which place one should give the impulsion and which is the size $\Delta v$.

This allows to obtain an elementary approach to a space mission. Later one can consider the effect of perturbations of other bodies, the separate effects of Earth and Moon, change to a non-planar target orbit, the fact that the target orbit is, approximately, quasiperiodic instead of periodic, to optimize wrt fuel consumption and wrt transfer time from departure to a vicinity of the target orbit, etc. For information about the methodology for the design and control of missions around libration points see [16, 17, 14, 15]. We detail the steps to find the solution in the present example.

**Step 1**. First we compute a periodic orbit around the Earth with period $\tau = 2\pi/366.25$. We start with initial data $(x_0, 0, 0, \dot{y}_0)$ and should require $\varphi_\tau(x_0, 0, 0, \dot{y}_0) = (x_0, 0, 0, \dot{y}_0)$. In fact, it is much simpler to ask for the image at $t = \tau/2$ to be of the form $(x_1, 0, 0, \dot{y}_1)$ and then the symmetry completes the task. We have two known data $x_0, \dot{y}_0$ and two conditions $y_1 = 0, \dot{x}_1 = 0$. After a few attempts one can use Newton method to find the solution $x_0 \approx -0.999714471273, \dot{y}_0 \approx 0.103463316596$. One can check that the monodromy matrix has a double eigenvalue equal to 1 (as expected: energy preservation and time shift) and the other eigenvalues are $\exp(\pm\alpha \mathrm{i}), \alpha \approx 0.034228998$. The difference wrt a circular orbit is less than 350 m. For further reference we denote as $\gamma(t)$ this orbit.

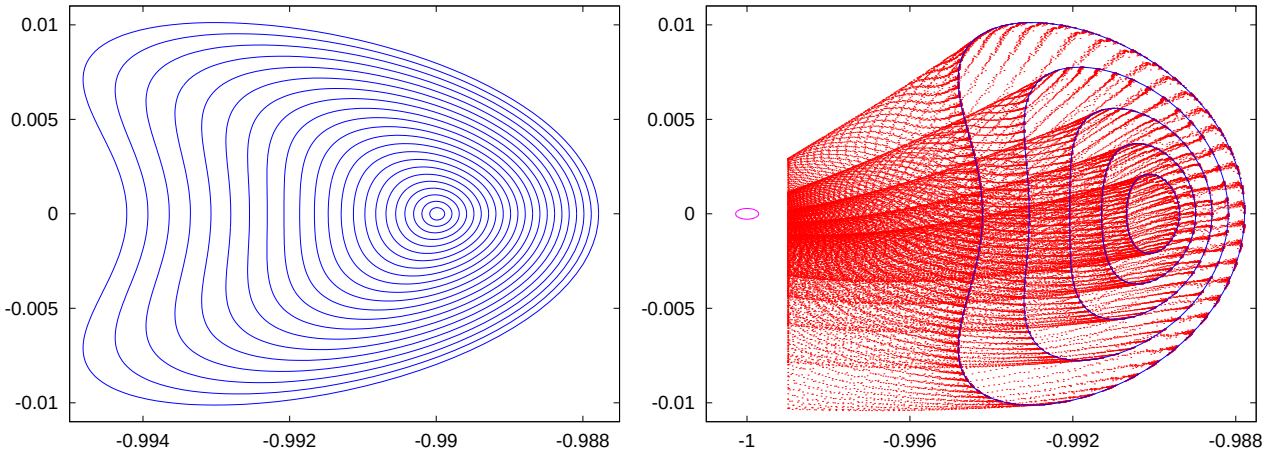


Figure 10: Left: some orbits in the family $\mathrm{hpo}_L$ around $L_1$. The initial values of $x$, on $y = 0$, are of the form $x_{L_1} + k \times 10^{-4}$ for $k = 1(1)22$. Right: For some of the orbits, concretely for $k = 6(4)22$, we plot also the left branches of $W^s_{PO_k}$ until they reach $x = -0.999$. In both plots the variables $x, y$ are shown.

**Step 2**. Now we face the $\mathrm{hpo}_L$ around $L_1$. First we locate $L_1$ by imposing $\Omega_x = 0$ as it follows from (24). Starting at $x = \mu - 1 + (\mu/3)^{1/3}$ Newton method converges quickly for $\mu$ small. Then we can compute the eigenvalues at that point, which turn out to be $\lambda, \lambda^{-1}, \exp(\pm\omega \mathrm{i})$ with $\lambda \approx 2.532659199, \omega \approx 2.086453579$. Hence, the maximal eigenvalue of the nearby periodic orbits, when they tend to $L_1$, is $\exp(2\pi\lambda/\omega) \approx 2052.671203$.

This large instability suggests, again, to look for the initial data for the $\mathrm{hpo}_L$ on the Poincaré section $y = 0$ for a fixed $x_0$ with $\dot{x}_0 = 0$ and leaving $\dot{y}_0$ as only unknown variable. The condition to be satisfied is then that the next intersection with $y = 0$ (to the left of $L_1$) should have $\dot{x} = 0$. This is easily solved by Newton method. From the half orbit we recover the full orbit by symmetry, the monodromy matrix and, hence, dominant eigenvalue and eigenvector. The instability becomes milder when the size increases. For instance, for the smallest orbit in Figure 10 left the dominant eigenvalue is 2050.987058, while for the largest one is 923.004416. Standard continuation techniques are used to generate these orbits.

**Step 3**. With the previously computed data it is simple to produce the left branches of the stable manifolds $W^{s,-}_{PO}$ of the $\mathrm{hpo}_L$ until they intersect the value $x = -0.999$. It is enough to use the linear approximation of the manifold in the Poincaré section $y = 0$. An example is shown in Figure 10 right. To compute the manifolds 200 points have been taken in a fundamental domain, equally spaced in logarithmic scale. The intersections for the orbits with $k = 8(2)22$, i.e., for the indices ranging from 8 to 22 with step 2, (see Figure 10) are shown in red in Figure 11 right, using $y, \dot{y}$ as variables.

**Step 4**. Last step is how to reach $W^{s,-}_{PO_k}$ for a given $k$ leaving from the parking orbit. It is suggested to give an impulsion $\Delta v$ from a given point $\gamma(t^*)$ in the orbit, in the direction of the velocity $\dot{\gamma}(t^*)$ at

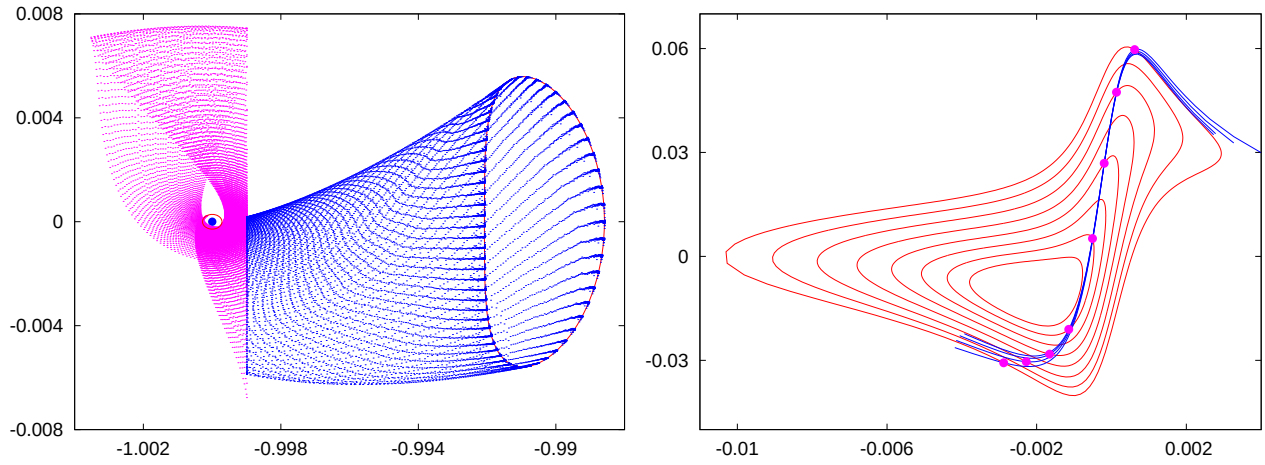


Figure 11: Left: The parking orbit and an example of a possible target $\mathrm{hpo}_L$ (with $k = 14$), both in red, the branch $W^{s,-}_{PO_{14}}$ in blue, and some of the possible trajectories $\psi(t, t^*)$ departing from the parking orbit (see text) in magenta. Plot done using $x, y$ variables. Right: The intersections of $W^{s,-}_{PO_k}$ for $k = 8(2)22$ with $x = -0.999$, in red, and the intersections with the same plane of $\psi(t, t^*)$ for different values of $t^*$ on the Jacobi levels of $PO_k, k = 10(4)22$, in blue. Note that these four blue curves are quite close and similar. The possible places for the transfer are the intersections of a $W^{s,-}_{PO_k}$ curve with the corresponding blue curve. They are marked in magenta. For each $k$ shown here two possible places are obtained. This plot is done using $y, \dot{y}$ variables.

that point. The first question is to compute which is the size of the new velocity. We simply require that the value of the Jacobi constant with this velocity equals the one of the target $PO_k$. Let $|v|$ the modulus obtained for this velocity. Then $\Delta v = |v| - |\dot{\gamma}(t^*)|$, and the components of the new velocity are proportional to the ones of $\dot{\gamma}(t^*)$. This allows to compute the trajectories $\psi(t, t^*)$ leaving from the parking orbit until they reach $x = -0.999$. Depending on $t^*$ it can happen that $\psi(t, t^*)$ reaches $x = -0.999$ or it goes first far away to the left spending too much time. These trajectories are skipped. A sample of the possible $\psi(t, t^*)$ trajectories for several $t^*$ values is shown in magenta in Figure 11 left, where the parking and target orbit (with $k = 14$) are in red and $W^{s,-}_{PO_{14}}$ is shown in blue.

Finally, on the right part of Figure 11 we show, in the $(y, \dot{y})$ variables, the information that has been obtained in $x = -0.999$: the intersections of $W^{s,-}_{PO_k}$ for $k = 8(2)22$, in red, and the intersections of $\psi(t, t^*)$ when one changes $t^*$, for the Jacobi levels of $PO_k, k = 10(4)22$, in blue. The intersections of a given red curve with the corresponding blue one are the candidates for the transfer. The values of $\Delta v$ are quite close. They range from 0.040286 for $k = 10$ to 0.041246 for $k = 22$ (i.e., impulsions ranging from 1.203 to 1.232 km/s).

## 4.2 Escape and confinement in the Sitnikov problem

This is an example to study escape/capture on a given problem of Celestial Mechanics using a very simple model. Two massive bodies of equal mass are moving on the $z = 0$ plane on elliptic orbits of eccentricity $e$ around the common centre of mass, located at $(0, 0, 0)$, with semimajor axis $a = 1$, while a body of negligible mass moves along the $z$ axis. The standing equations are

$$\ddot{z} = -\frac{z}{(z^2 + r(t)^2/4)^{3/2}}, \quad r(t) = 1 - e\cos(E), \quad t = E - e\sin(E), \tag{26}$$

where $E$ denotes the eccentric anomaly of the primaries. For $e = 0$ the problem has 1 dof and, hence, it is integrable. As a first order system we have $\dot{z} = v$, $\dot{v} = z(z^2 + r(t)^2/4)^{-3/2}$, with the obvious symmetries $S_1 : (z, v, t) \leftrightarrow (z, -v, -t)$, $S_2 : (z, v, t) \leftrightarrow (-z, v, -t)$, $S_3 : (z, v, t) \leftrightarrow (-z, -v, t)$. We can introduce $E$ as new time variable (denoting $' = d/dE$) and introduce a Hamiltonian formulation:

$$H(z, E, v, J) = (1 - e\cos(E))\left[\frac{1}{2}v^2 - (z^2 + (1 - e\cos(E))^2/4)^{-1/2}\right] - J.$$

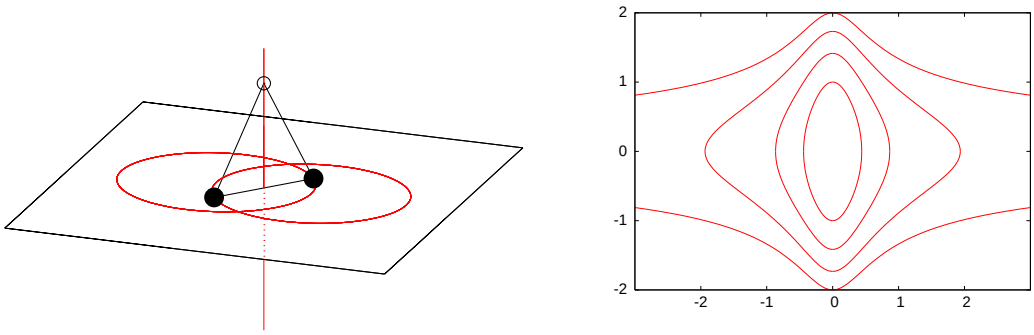


Figure 12: Left: A representation of the Sitnikov model. Right: For $e = 0$ plots of the orbits in the $(z, v)$ variables for values of $H$ equal to $-1.5$, $-1.0$, $-0.5$ and 0.

A suitable Poincaré section for the representation of orbits is $\Sigma = \{z = 0\}$ and to use $(v, E)$ as local coordinates. Thanks to the symmetry and to avoid strong deformations we shall use, instead, $(\hat{v}, E)$, where $\hat{v} = |v|(1 - e\cos(E))^{1/2}$.

If the infinitesimal mass escapes to infinity, the massive bodies move in $\mathbb{S}^1$ (eventually, after regularization of binary collisions using Levi-Civita variables). One talks of a periodic orbit at infinity. A celebrated Theorem by Moser states

**Theorem 4.1.** *The problem has periodic orbits at both $z$ plus and minus infinity, with invariant manifolds (orbits going to or coming from infinity parabolically). For $e$ small enough the manifolds intersect $\Sigma$ in curves diffeomorphic to circles. These curves have transversal intersection, implying the existence of heteroclinic orbits from $+\infty$ to $-\infty$ and vice versa.*

As a consequence one has: non-integrability, embedding of the shift with infinitely many symbols, existence of oscillatory solutions, escape/capture domains, etc. The PO at $\infty$ is parabolic or, topologically, weakly hyperbolic. The linearized map around the PO is the identity. To study the vicinity of these orbits we introduce McGehee variables $(q, p)$ defined as $z = 2/q^2, \dot{z} = -p$. Then the equations of motion become

$$q' = \Psi q^3 p, \quad p' = \Psi q^4 \left(1 + \Psi^2 q^4\right)^{-3/2} \quad \text{being} \quad \Psi = (1 - e\cos(E))/4. \tag{27}$$

If $e = 0$ the invariant manifolds are given as $p = \pm q(1 + q^4/16)^{-1/4}$. We shall denote as $W^{u,s}_{\pm}$ the intersections of unstable/stable manifolds of $\pm\infty$ with $\Sigma$. Due to $S_3$, $W^u_{\pm}$ coincide and also $W^s_{\pm}$ coincide, but $W^s_+, W^u_-$ have $v > 0$, while $W^s_-, W^u_+$ have $v < 0$. Due to $S_1$, $W^u_+$ and $W^s_-$ are symmetric with respect to $E = 0$.

We look for a parametric representation of the manifolds of the PO as

$$p(E, e, q) = \sum_{k\geq 1} b_k(e, E) q^k = \sum_{k\geq 1} \sum_{j\geq 0} \sum_{i\geq 0} c_{i,j,k} e^i \,\mathrm{sc}(jE)\, q^k, \tag{28}$$

where $b_k(e, E)$ are trigonometric polynomials in $E$ with polynomial coefficients in $e$, $c_{i,j,k}$ are rational coefficients and sc denotes sin or cos functions.

Note that the problem can be reduced to obtain invariant manifolds of fixed parabolic points of discrete maps (think about the intersection of the manifolds with $E = 0$). In this context McGehee proved [25]: The invariant manifolds are analytic except, perhaps, at $q = 0$. In fact, a result of Baldomà and Haro [1] shows that, generically, the 1-dimensional manifolds of fixed parabolic points are of some Gevrey class (see section 2.1.2).

From (27) and (28) the invariance of the manifolds can be written as

$$\Psi q^4 \left(1 + \Psi^2 q^4\right)^{-3/2} = \sum_{k\geq 1} \frac{db_k}{dE}(e, E) q^k + \sum_{k\geq 1} b_k(e, E) \Psi k q^{k+2} \sum_{m\geq 1} b_m(e, E) q^m. \tag{29}$$

Equating coefficients of powers of $q$ in (29) leads to the recurrence

$$\binom{-3/2}{m} \left(\frac{1 - e\cos(E)}{4}\right)^{2m+1} = b'_n(e, E) + \frac{1 - e\cos E}{4} \sum_{k=1}^{n-3} k b_k(e, E) b_{n-2-k}(e, E), \tag{30}$$

where $m = n/4 - 1$, defined only for $n$ multiple of 4.

To solve the recurrence in (30) we first note that for the unstable manifold of $+\infty$ we have $b_1 = 1$. One has $b_1 = -1$ for the stable manifold. For a given value of $n$ we can split the function $b_n$ as $\tilde{b}_n + \bar{b}_n$, where $\bar{b}_n$ denotes the average and $\tilde{b}_n$ the periodic part. Given $b'_n(e, E)$ equal to some known function (computed from the previous coefficients) allows only to compute the periodic part $\tilde{b}_n$. The average $\bar{b}_n$ is computed previous to the solution of the equation for $b'_{n+3}(e, E)$, to have a zero average function when we integrate. An essential fact is that $b_2 = b_3 = b_4 = 0$. One has also $b_6 = b_7 = b_{10} = 0$, but this is not so relevant.

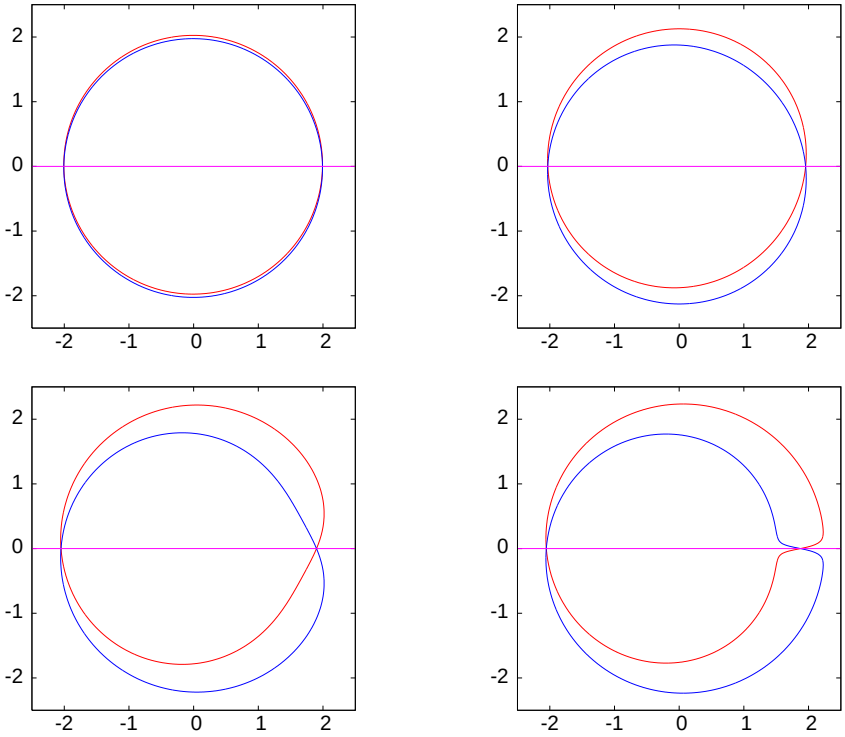

Figure 13: The manifolds $W^u_+$, in red, and $W^s_-$, in blue, for different values of $e$. At the top row for $e = 0.1$ (left) and $e = 0.5$ (right) and at the bottom row for $e = 0.9$ (left) and $e = 0.999$ (right). In all cases we use $(\hat{v}, E)$ as polar coordinates.

Now it is a simple task to implement the computation of the coefficients to high order. Using high order is important, because this allows to have a good representation for large values of $q$. A large $q$ allows to start the numerical integration, to obtain the intersection $W^u_+$ of the manifold with $z = 0$, at a moderate value of $z$. For instance, using terms up to order $n = 100$ one checks that the representation is good (error of the order of $10^{-16}$) for $q = 1/3$. Then the numerical integration can be started at $z = 2/q^2 = 18$.

The Figure 13 shows some results for different values of $e$, displaying $W^u_+$ and $W^s_-$ and using the $(\hat{v}, E)$ variables as polar coordinates. Note that the use of $(|v|, E)$ would give curves extremely elongated to the right for $e$ close to 1. Concretely, if the eccentricity is equal to $1 - \delta$ then the horizontal variable in the plots reaches values $\approx 2/\sqrt{\delta}$. The values of the splitting angle at $E = 0$ and $E = \pi$ on the section $\Sigma$ are shown as a function of $e$ in Figure 14. Note the quite different behaviour when $e \to 1$. This gives evidence of the transversality for all values of $e$.

Summarizing: the steps to obtain the manifolds $W^u_+$ and $W^s_-$ and, hence, the splitting angle, are

1) Introduce McGehee coordinates to pass from (26) to a formulation around the periodic orbits at infinity, as given by (27).

2) Look for a suitable representation as the one in (28), in which the manifold is expressed as function of a distance to infinity ($q$) and a periodic time variable ($E$). Write the invariance condition (29) and derive the recurrences, as given in (30).

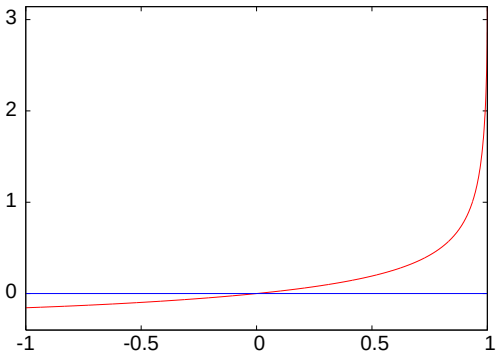


Figure 14: The splitting angle of the manifolds $W^u_+$ and $W^s_-$ in $\Sigma$. For positive values on the horizontal axis the splitting angle at $E = 0$ is shown as a function of $e$. For the negative ones, the splitting angle at $E = \pi$ is shown as a function of $-e$.

3) Analyze the properties of the recurrences (symmetries, powers of $e$ in the coefficients of the trigonometric polynomials, etc). Design and implement routines to obtain the desired numerical coefficients.

4) Select a suitable value of $q$ for the current maximal order of the expansion, evaluate (28) for a sample of values of $E$ for every desired value of $e$ and carry out the numerical continuation until $z = 0$.

It is important to stress that for other similar problems (RTBP planar or spatial, general, etc) to decide if an observed body will be captured or will escape, it is enough to obtain the manifolds and decide the actual position with respect to them.

## 4.3 Practical confinement around triangular points

As mentioned at the beginning of section 4, the triangular libration points are linearly stable in the 3D RTBP if $\mu$ is small enough. But, what can be say about nonlinear stability? For the 2D case nonlinear stability is proved for $\mu \in [0, \mu_1)$ except for the couple of values $\mu_2, \mu_3$. A possible approach is to reduce to the study of a symplectic 2D map and to apply Moser theorem. There is an exceptional value for which the twist condition is not satisfied, but can be recovered as a *weak twist* to higher order via normal forms.

In the 3D case, in principle, there is no way to avoid diffusion. Hence, initial conditions as close as we like to $L_{4,5}$ can go far away from that point. But normal forms, or averaging, lead to the already mentioned Nekhorosev estimates, showing that one needs an extremely large time if one starts close enough to the libration point as discussed in section 3.5.

But these results, concerning domains of practical stability in the 3D case give, at most, small regions around the triangular points. On the other hand one has found the so-called Trojan (and Greek) asteroids, for the Sun–Jupiter system, far away from $L_{4,5}$, even with relatively high inclination. Hence, it seems that the domain of practical stability for long times is much larger than what is given by theoretical predictions. It would be nice to search for the confining mechanisms.

A side problem is why Trojan-like bodies are not found in the Earth-Moon case. Certainly the Sun is guilty for that, the orbits equivalent to $L_{4,5}$ for the E-M system being unstable even in simple models of the E-M-S motion. But this do not excludes the possibility that stable orbits exist with moderate inclination.

Here we present some results which can help to understand the main mechanisms, see [45].

For different reasons many computations are done with initial conditions on the ZVS using $(z, \alpha, \rho)$ as parameters for a fixed $\mu$, as follows:

$$x = \mu + (1+\rho)\cos(2\pi\alpha), \quad y = (1+\rho)\sin(2\pi\alpha), \quad z = z_0 \geq 0, \quad \alpha \in (0, 1/2), \quad \dot{x} = \dot{y} = \dot{z} = 0. \tag{31}$$

As for $\mu = 0$ one must be in $1-1$ resonance it is convenient to look, starting at the ZVS, for initial conditions at rest, in the synodical frame, in the moment that an elliptic orbit with semimajor axis equal

to the unity passes through the apocentre in the sidereal frame. That is, for values of $(z, R = 1 + \rho)$ related by

$$z = \left[4(1+R^2)^{-2} - R^2\right]^{1/2} \quad \text{or} \quad \psi = 1 - \frac{1}{2}w + \frac{3}{2^5}w^2 - \frac{1}{2^8}w^3 - \frac{25}{2^{13}}w^4 + \frac{33}{2^{16}}w^5 + \mathcal{O}(w^6), \tag{32}$$

where $w = z^2$, $\psi = \psi(z) = R^2$. This suggests to make plots using the variables

$$(\alpha,\ \gamma = 1 + \rho - \sqrt{\psi(z)},\ z). \tag{33}$$

It is clear that $L_5$ corresponds to $\rho = 0, \alpha = 1/3, z = 0$. By symmetry, similar results are obtained for $L_4$. Also by symmetry it is enough to look for $z \geq 0$. For the limit case, $\mu = 0$, one would have $\gamma = 0$.

Some reasons to start at the ZVS are:

- Most of the i.c. non-leading to escape are on 3D tori. Hence, we scan a set of positive measure in the full phase space (not fixing the Jacobi constant $C$).
- The results obtained can be used as a seed to obtain the relevant objects involved in the practical confinement, either starting at the ZVS or not.

First we show some results concerning the *quasi-boundary* between escape and practical confinement. In Figures 15 and 16 we display, for a small value $\mu = 10^{-4}$ of the mass parameter, two different kinds of objects which appear on the quasi-boundary. We should mention that the relevant objects have codimension 1 in the full phase space. In present case they have dimension 5. Typically they are $W^{u,s}$ of central objects of dimension 4. These objects can be the centre manifolds of fixed points of centre×centre×saddle type or the centre manifolds of 1-parameter families of periodic orbits of centre×saddle type (the parameter being, e.g., the value of the Jacobi constant). But it is clear that these $W^{u,s}$ do not coincide: there is some splitting. This is the reason why they are named quasi-boundaries.

We note, for instance, that in the upper left plot of Figure 16 beyond the blue curve commented on the caption, one can guess another invariant curve (in the Poincaré section, a 2D torus in the phase space) on top of the plot. The separation between confined and escaping orbits is close to a double heteroclinic connection between the lower curve in blue and the upper one in red. But the related branches of these two partially normally invariant curves do not match exactly. There is some tiny splitting between the branches.

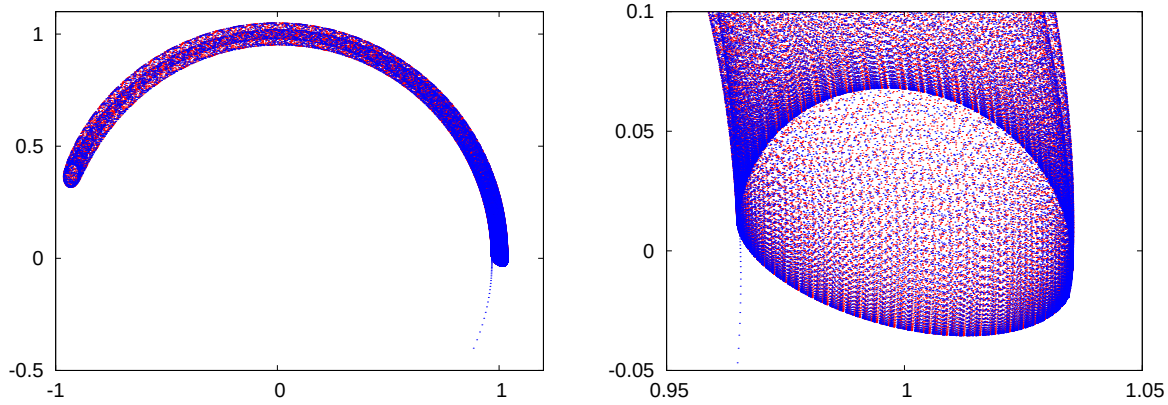


Figure 15: Example of a transition for $\mu = 0.0001$, $\alpha = 0.05$, $z = 0.3$. The two tori (confined in red, escaping in blue) have values of $\rho$ which differ in $10^{-10}$ We show the projections on $(x, y)$ of the Poincaré section through $z = 0$. Left: a global view. Right: a magnification. The separating unstable 2D torus or invariant curve in the section, belongs to $W^{u,s}_{L_3}$. Note that the points in red are partially hidden by the ones in blue.

In Figure 17 we display a general view of the boundary. See comments on the caption. Typically the transitions have been detected after a maximum integration time equal to $10^6 \times 2\pi$ (in special cases 10, $10^2$ or $10^3$ times larger) and with a resolution of $10^{-6}$ in $\rho$. See slides 4. on the web for other values of $\mu$.

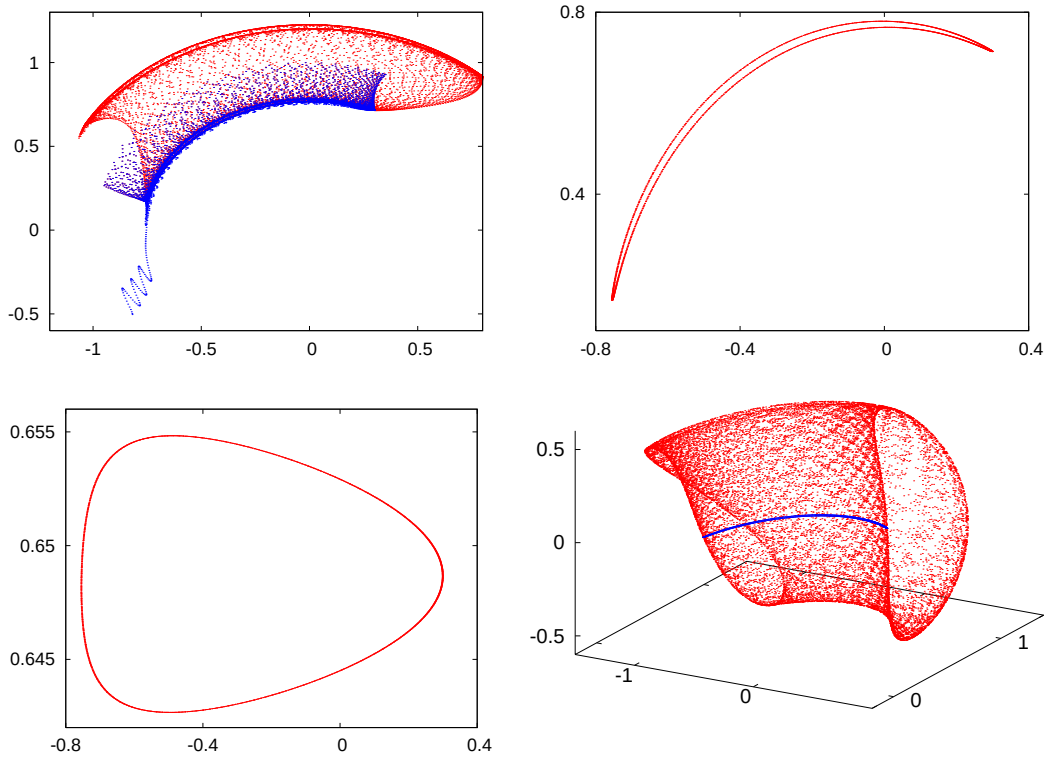


Figure 16: Similar to Figure 15 but starting at $\alpha = 0.4$, $z = 0.6$. Now the separating unstable 2D tori are not in $W^{u,s}_{L_3}$. Top: initial part of Poincaré iterates with many iterates in blue, giving evidence of the lower unstable 2D torus and points escaping from it (left) and the separating lower unstable invariant curve alone (right) projected on $(x, y)$. Bottom: The same curve projected on $(x, \dot{z})$ (left) and the related 2D separating unstable torus in a $(x, y, z)$ projection.

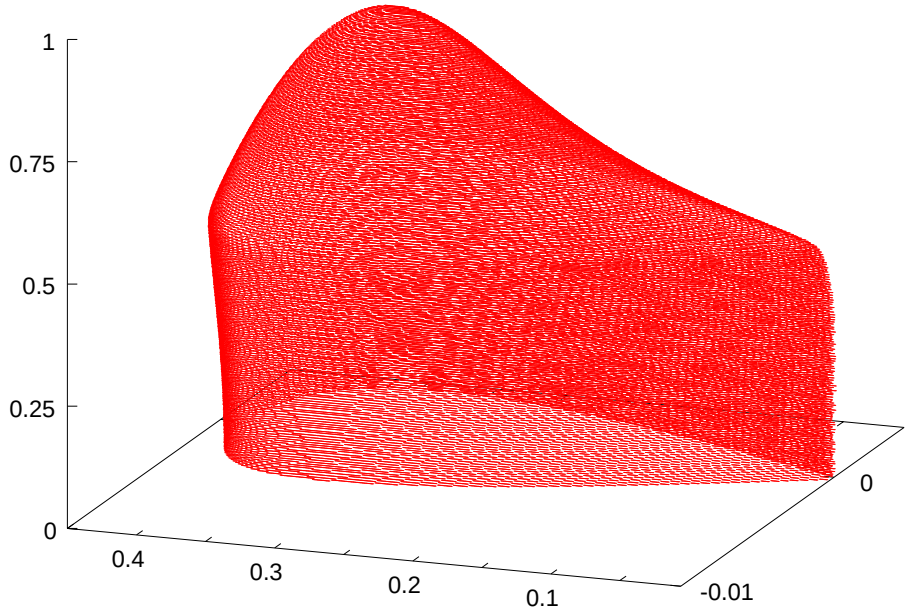


Figure 17: A 3D view of the detected boundaries of practical stability starting at the ZVS for $\mu = 10^{-4}$, shown in the $(\alpha, \gamma, z)$ variables. The inner (resp., outer) part corresponds to $\gamma < 0$ (resp. $\gamma = 0$). Note the sharp change on the behaviour of the boundary which occurs between $z = 0.4$ and $z = 0.5$.

We can make a rough scan of the boundaries for different values of $\mu$, both for the planar and spatial RTBP. We say rough in the sense that, typically, the maximal time to look for escape has been reduced to $10^5 \times 2\pi$ time units and that the grid we scan uses $\Delta\rho = 10^{-4}$, then $\Delta\alpha$ equal to $2 \times 10^{-4}$ in the planar case ($5 \times 10^{-4}$ in the spatial one) and $\Delta z = 5 \times 10^{-3}$ in the spatial case. The results are shown in Figure 18. Note that the effect of the resonances is less important in the spatial case. This is due to the fact that for some values of $\mu$ the resonances destroy stability in the planar case, but still a large set of initial conditions is stable in the spatial case. The change of the frequencies when $z$ increases is responsible for the minima being shifted to larger values of $\mu$.

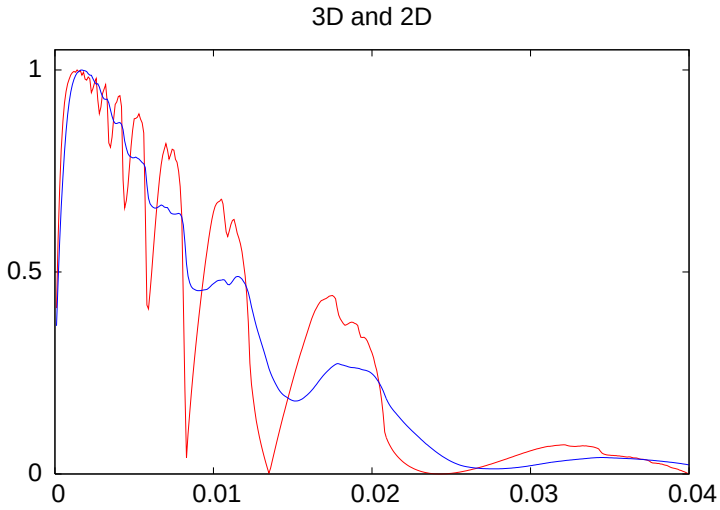


Figure 18: Statistics as a function of $\mu$ starting at the ZVC (planar case, in red) and at the ZVS (spatial case, in blue). This is normalized to the maximum, which for the planar case occurs at $\mu = 0.0014$ with 282757 points. For the spatial case it occurs for $\mu = 0.0017$ with 19014882 points. Note the sharp effect of the resonances in the planar case. Similar patterns are found for the Hénon map and in many other examples, see [43]. In the spatial case the effect of the resonances is milder and delayed. In both cases some stability subsists even for $\mu > \mu_1$.

From now on we concentrate on a fixed value $\mu = 0.0002$. The reasons for the choice are:

- Being $\mu$ small, the boundaries are sharper,
- It should be also possible to obtain some information by means of perturbation theory,
- It is close to the Titan-Saturn mass ratio.

This small value of $\mu$, however, raises a problem: The escape is relatively slow and, hence, the integration time is large.

The methodology used (for the $L_5$ case) is as follows:

1) Define some escape criterion (e.g., the $(x, y)$ projection of the orbit enters some wedge near the negative $y$ axis, or the orbit comes too close or too far from the primary, or too close to the secondary).

2) Scan a set of initial conditions for short time (e.g. $10^4 \times 2\pi$, using some grid with small steps $\Delta\alpha, \Delta\rho, \delta z$). Look at every initial point on the grid, for fixed $z$, as a pixel. Keep the pixels non leading to escape.

3) Repeat for longer time (e.g. $5 \times 10^4 \times 2\pi$) for the pixels at a distance (counted in the sup norm) less than $d$ pixel units from the ones which already escaped (typically we take $d = 5$). The tested points are marked depending on whether they escape or they remain. Iterate the scan until no more points have to be tested: all the ones at distance $\leq d$ from escaping points have been tested and remain. Repeat two more times for longer and longer integration time ($25 \times 10^4 \times 2\pi$, $10^6 \times 2\pi$).

4) Eventually do additional refinements of $\rho$ for fixed $\alpha, z$.

Figures 19 and 20 show some results for $\mu = 0.0002$, displaying, for different values of $z$, the set of non-escaping points starting on the ZVS and the boundaries of the domain. See the captions for the variables used to represent the results. Note that the domain of practical stability contains, for the planar case $z = 0$ stable points quite close the $L_3$ ($\alpha \approx 0$). In the spatial case there are stable orbits which reach $z$ as large as 0.865 and, as the value of $\rho$ for these orbits reaches $\approx -0.181$ they have a maximum inclination exceeding 46 degrees.

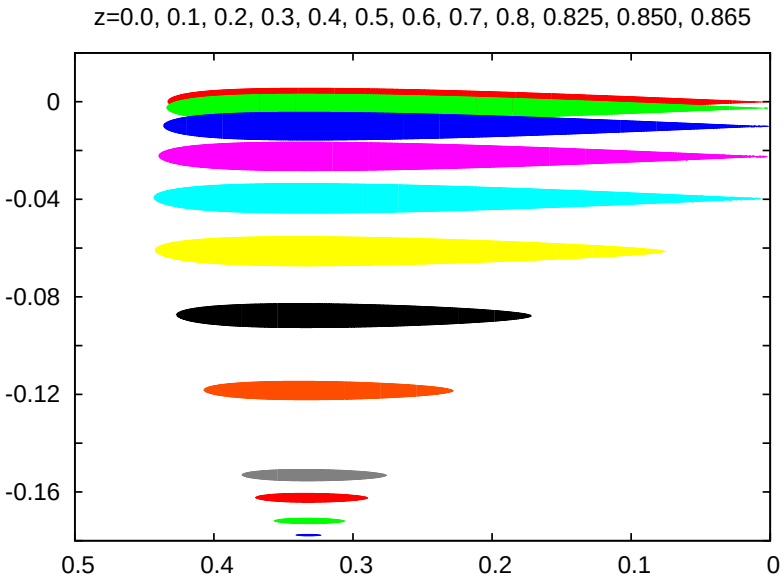


Figure 19: For $\mu = 0.0002$ the subsisting points, starting at the ZVS for 12 different $z$ values, given on the top of the plot. The coordinates used for the representation are $(\alpha, \rho)$.

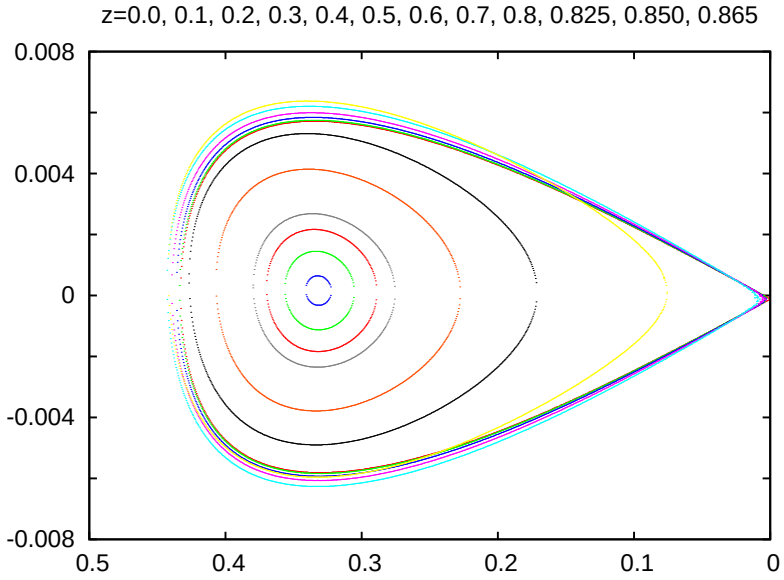


Figure 20: Boundaries of the domains shown in Figure 19 using the paraboloid like corrections. That is, as vertical variable one has used $\gamma$, as defined in (33) instead of $\rho$.

Still many things must be completed even for this small $\mu$ for which the boundaries tend to be rather sharp, because they are associated to relatively small splitting. The problem becomes more rough for the Sun-Jupiter case, because then one starts to see the effect of some island-like structure. For the Earth-Moon case the behaviour is quite wild due to the strong effect of resonances. The Earth-Moon mass ratio is not far from the 3:1 resonance value $\mu_3$.

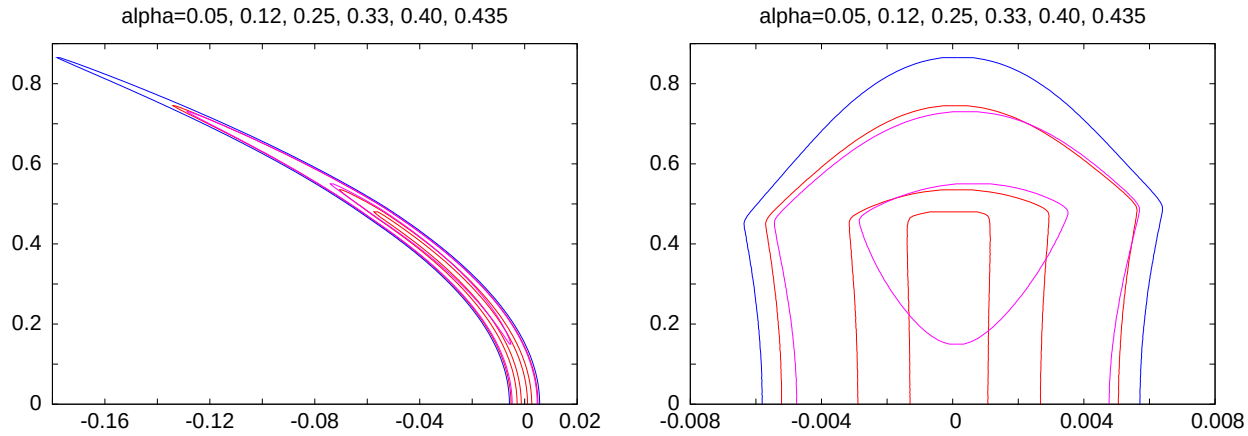


Figure 21: Some sections of the boundary starting at the ZVS for different values of $\alpha$. Left: in the $(\rho, z)$ variables. Right: using the $(\gamma, z)$ variables. In red are plotted the curves for $\alpha = 0.05, 0.12, 0.25$, easily seen on the right plot going away from $(0, 0)$ and each line encircling the previous one. In blue the curve for $\alpha = 0.33$ is displayed. This is the largest one. Finally the curves for $\alpha = 0.40$ and $\alpha = 0.435$ are plotted in magenta. Last one do not reaches $z = 0$.

## 4.4 Infinitely many choreographies in the 3-body problem

In the Newtonian $N-$body problem with all masses equal to 1 we can consider very simple solutions in the planar case, like $N-$gon relative equilibrium solutions. Due to the homogeneity one can scale time and distance so that it is enough to consider solutions with period $2\pi$. The $N$ bodies move on a circle of radius $R$ such that

$$2R^3 = \Sigma_{j=1}^{N-1}(2\sin(j\pi/N))^{-2}.$$

It is clear that all the bodies move on the same path in the plane. Hence, a natural question is: Are there other periodic solutions such that all bodies with equal masses move on the plane along the same path? At the end of the XXth century a solution with 3 bodies on the same planar curve, different form a circle, was proved to exist by Chenciner and Montgomery [5]. Also Moore [30] found the same orbit in a previous numerical work in a different context, a few years before. The path of this solution is the very popular figure eight curve and is displayed in Figure 22.

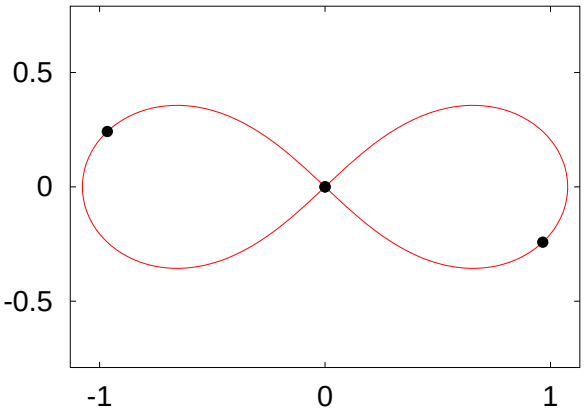


Figure 22: The figure eight solution of the 3-body problem. The initial positions of the bodies are marked as black points. For concreteness we can assume that at $t = 0$ the body located at the origin moves to the right, up. This forces the motion of the other two.

Immediately one can pose the question for $N > 3$ and for other shapes of the path. These solutions are named choreographies because of the dancing-like motion of the bodies, seen in animations, see [41, 6]. More precisely they should be named simple choreographies, because they are on the same curve. $k$-choreographies has to be used for bodies moving on $k$ different curves. Slides 6. provide some examples

and links to animations. One can also introduce the notion of relative choreographies if they are seen as choreographies in a uniformly rotating frame. Two choreographies which differ only by a rotation, by scaling, change of orientation, symmetry, etc, should be seen as the same.

Returning to simple choreographies in a fixed frame (or absolute choreographies) what one tries to find is some $2\pi$–periodic function $\psi : \mathbb{S}^1 \mapsto \mathbb{R}^2$ such that if the body $j$ is located at $q_j(t) = \psi(t-(j-1)2\pi/N)$ for $j = 1, \ldots, N$, we have a solution to the equations of motion.

Another natural question arises: Are there other choreographies of the 3-body problem different from the figure eight?

A simple observation is that at some $t > 0$, relatively small, the three bodies in Figure 22 will be in an isosceles configuration. Such a configuration is defined, for instance, assuming that at some moment of time the bodies 2 and 3 have positions and velocities given by

$$x_3 = x_2, \quad y_3 = -y_2, \quad \dot{x}_3 = -\dot{x}_2, \quad \dot{y}_3 = \dot{y}_2. \tag{34}$$

The conditions for $m_1$ are determined from the centre of mass integrals. This isosceles triangle has a symmetry axis passing through $m_1$.

Assume that after some time $\tau$ the bodies pass through another isosceles configuration, concerning positions, with the body $m_2$ in the symmetry axis defined by the positions of $m_3$ and $m_1$ and that the velocities are close to satisfy the isosceles condition. Let $\beta$ be the angle between the former symmetry axis (the $x$ axis) and the new one. A refinement is done to satisfy the full isosceles conditions with good accuracy (see the end of this subsection). Then, after rotating positions and velocities at $\tau$ by an angle $-\beta$, we have an isosceles configuration with the same symmetries concerning velocities than the initial one. The only change is a circular permutation of the bodies with change of orientation. Then the action of the semi-direct product of $\mathbb{Z}_2$ and $\mathbb{Z}_3$ (symmetry and permutation of the bodies) produces a relative choreography with period $T = 6\tau$ and rotation $6\beta$. If $\beta$ is $k\pi, k \in \mathbb{Z}$, we have an absolute choreography, symmetric with respect to the $x$ axis.

This has been applied to $\approx 10^9$ initial conditions. Near $3\times10^5$ relative choreographies have been found and by continuation of each one of them with respect to the angular momentum many (345 up to now) absolute, non-equivalent, choreographies have been found. It is clear that several relative choreographies can lead, by continuation, to an absolute choreography equivalent to another one found previously and they are not counted. It is checked that some of these new 3-body choreographies seem to belong to families. An example is shown in Figure 23. See [42] for other families.

Figure 23 suggests to try to continue the family for an increasing number of loops. Now the continuation has to be done with respect to integers and not in a continuous way. But using extrapolation of the data from the previous loops it has been possible to continue the family without any problem (using quadruple precision and high order extrapolation) until the solution shown in Figure 24. The natural conjecture is that there are infinitely many choreographies in this family.

There is an easy description of that solution. One of the bodies (say, the red one) moves close to an elongated ellipse while the other two (green and blue) move in a close binary, with its centre of mass close to an ellipse. When the three bodies approach the centre of mass there is an exchange: the blue body moves close to a elongated ellipse and the red and green form a binary in turn. At the end of this we have traveled 1/3 of the period. The bodies return to the initial position with a cyclic permutation RGB $\rightarrow$ GBR. One should stress that when they approach the centre of mass the bodies are not close to triple collision. Preliminary results seem to indicate that the minimal value of the moment of inertia along the orbit is strictly decreasing with the number of binary loops, tending to a positive constant.

It should be mentioned that among the 345 absolute choreographies available, one can identify several families. It is not excluded that some of these families contain infinitely many elements. But it can also happen that a couple of families merge together in a saddle-node bifurcation.

The steps for that application are as follows:

1) To obtain initial data in isosceles configuration one can prescribe some negative energy. Then we give values of $(x_2, y_2)$ and determine the positions of the other masses. Because of the symmetries we can select $x_2 > 0, y_2 < 0$. A bound on the domain is obtained because the kinetic energy should be non-negative. The possible values of the $(\dot{x}_2, \dot{y}_2)$ are parametrized by an angle $\gamma \in [0, 2\pi]$.

2) Then we proceed to the integration of (1) with the selected initial conditions, looking for a passage near another isosceles configuration. A maximal time is used (e.g. 5 units) and the attempt is stopped if the bodies move too far or they become too close. If a candidate is obtained a refinement is done by Newton method, to have a good approximation to an isosceles symmetry after 1/6 of the period. For the refinement we fix $\gamma$ and leave $(x_2, y_2)$ as free variables to satisfy the isosceles condition for the velocities when it is satisfied by the positions.

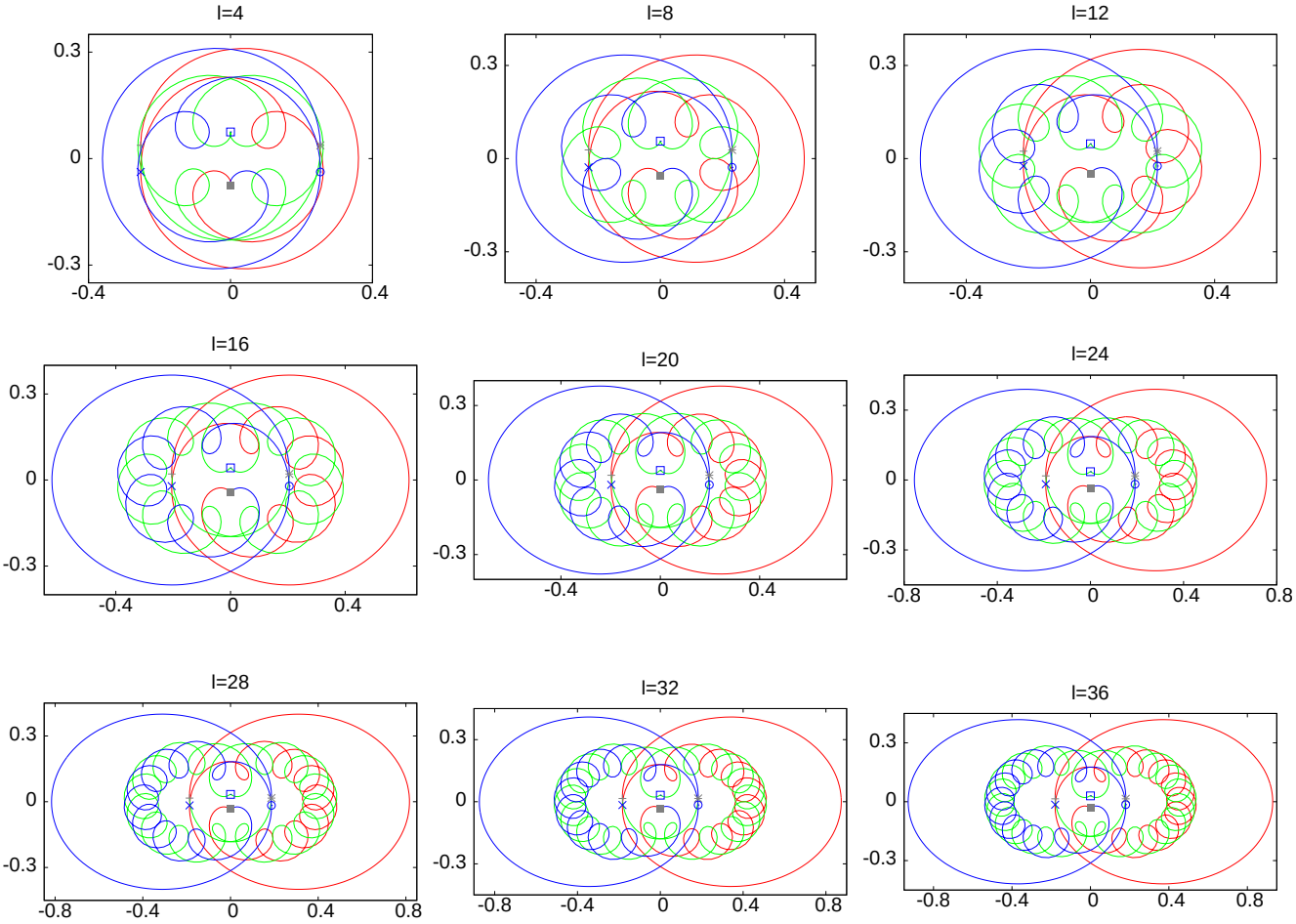


Figure 23: Choreographies of the 3-body problem belonging to a family. The paths of the three bodies during 1/3 of the period are shown in different colors. The positions of the bodies in the initial isosceles configuration and the ones after 1/6 of the period are also shown. To display the solutions with the same scale in $x$ and $y$ variables, the coordinates have been exchanged. Now, for these choreographies, the symmetry axis is the vertical one and for this family both isosceles configuration (at $t = 0$ and after 1/6 of the period) are symmetrical the one from the other wrt the horizontal axis. Counting the little inner loops (for instance, the ones in red) the number increases from 1 to 9 from top to down and from left to right. The value $\ell$ on top of each plot refers to the total number of small loops, either in red, blue or green.

3) Next we carry out continuation by changing the angular momentum, looking for an absolute choreography. Continuation is stopped if the bodies approach a collision. The new absolute choreographies are stored in a list. If they are already in the list, they are discarded. Later, for our present goal, we select the ones which belong to the family as shown in Figure 23.

4) Finally the family is continued wrt the number of loops. An extrapolation based on the previously computed loops allows to have a very good guess. Then Newton method converges in few iterations.

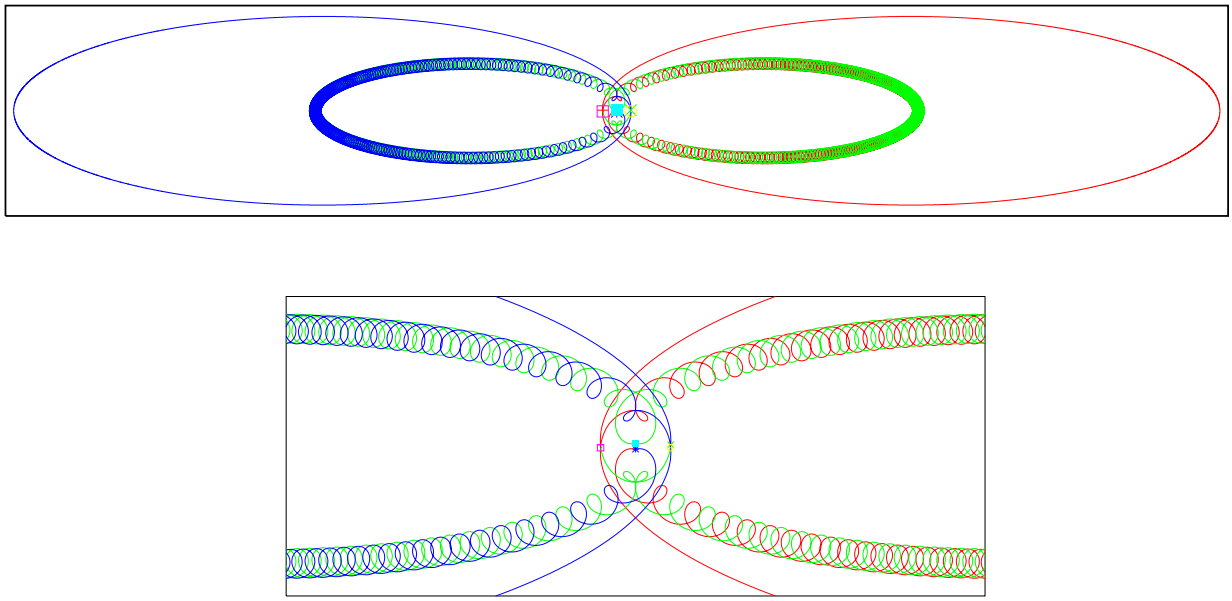

Figure 24: Top: a choreography of the 3-body problem of the same family of the ones shown in Figure 23. In each of the binary portions the bodies in the binary make 200 revolutions around the centre of mass of the binary, while the third body moves close to an elongated ellipse. Only 1/3 of the orbit is shown. The remaining parts are obtained by cyclic permutations. Bottom: a magnification of the central part of the top.

## 4.5 Evidences of diffusion related to the centre manifold of $L_3$

In this last application we consider the 3D RTBP for a small value $\mu = 0.0002$, like we used in subsection 4.3. Our goal is to give evidences of the diffusion when we consider the unstable dynamics originated by the unstable/stable manifolds of the part $W^c_{L_3,C}$ of the centre manifold $W^c_{L_3}$ of $L_3$ for a given value $C$ of the Jacobi constant. For concreteness we use the value $C = 2.95998466228$. To have a feeling of the meaning, let us say that for that value of $C$ the $\text{vpo}_L$ in $W^c_{L_3,C}$ has values of $z$ going from $-0.2$ to $+0.2$.

Beyond the $\text{vpo}_L$ the $W^c_{L_3,C}$ contains 2D tori, the $\text{hpo}_L$, some tiny chaotic domains and the additional periodic orbits related to these domains. Using the methods of subsection 3.1 and 3.3 we can compute both periodic orbits and several tori. It is simpler to represent the tori as IC of the Poincaré map $\mathcal{P}$ associated to the section $\Sigma := \{z = 0, \dot{z} > 0\}$. In this application we shall use once and again $\Sigma$ and $\mathcal{P}$. As we fixed also the value of $C$, we have to consider a discrete map in a 4D space that we denote as $\Sigma_C$.

The IC are hyperbolic normally to the centre manifold. Hence, we can compute its manifolds, say $W^u_{\mathcal{C}}, W^s_{\mathcal{C}}$, for a given curve $\mathcal{C}$. Note that these manifolds are 2D and to visualize them we can compute a section through some codimension-1 manifold in $\Sigma_C$ (e.g., an hyperplane $\Pi$). A suitably chosen $\Pi$ gives as $W^u_{\mathcal{C}} \cap \Pi$ a closed curve, say $\mathcal{C}_u$. In a similar way we can obtain $\mathcal{C}_s$. Of course, these two curves in $\Sigma_C \cap \Pi$, which is 3D, do not intersect generically, as opposite to $W^u_{\mathcal{C}}$ and $W^s_{\mathcal{C}}$ which are 2D in the 4D space $\Sigma_C$, for which one expects to have intersections, but not necessarily located in $\Pi$. But we can have a feeling of their relative position by looking at $\mathcal{C}_u$ and $\mathcal{C}_s$.

Figure 25 illustrates what has been said. In the left plot several IC are shown, as well as the point corresponding to the $\text{vpo}_L$. Note that the largest IC is quite close to the $\text{hpo}_L$. The 2D torus corresponding to this last IC has values of $z$ which range in the small interval $[-0.017, 0.017]$. The $\text{hpo}_L$, which is contained in $z = 0$, is located outside the largest IC shown at a distance $\approx 0.004$. The right plot displays $\mathcal{C}_u$ and $\mathcal{C}_s$ for several IC, using as $\Pi$ the hyperplane defined by $y = -\sqrt{3}(x - \mu)$. One detects, visually, that for tori close to the $\text{vpo}_L$ the curves are quite close. The difference increases going outside, away from the $\text{vpo}_L$, and decreases again when approaching the $\text{hpo}_L$. This will be one of the relevant facts to explain the results obtained.

Figure 26 shows the projection in $(x, y)$ of the first $10^5$ iterates under $\mathcal{P}$ starting at a point close to the blue curve, say $\mathcal{C}_b$, in Figure 25, left. The first iterates follow closely the upper part of $W^u_{\mathcal{C}_b}$ and

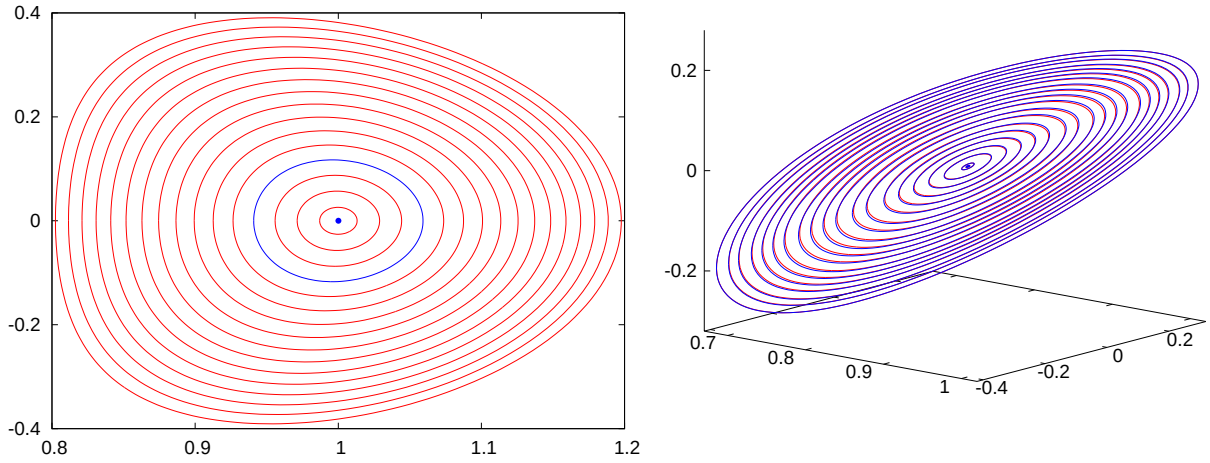


Figure 25: Left: Invariant curves obtained as intersections with $\Sigma$ of some tori in the $W^c_{L_3,C}$ for $C = 2.95998466228$ projected on the $(x, y)$-plane. The $\mathrm{vpo}_L$ orbit for this value of $C$ has $z \in [-0.2, 0.2]$ and corresponds to the blue point. The blue curve will be used in the computations reported here. Right: Sections with $y = -\sqrt{3}(x - \mu)$ of the Poincaré sections of the unstable (red) and stable (blue) manifolds of some of the tori. For the 3D view we use the $(y, \dot{y}, \dot{z})$ variables.

return near $\mathcal{C}_b$ close to the upper part of $W^s_{\mathcal{C}_b}$ (or of some other nearby curve). As it is well known, next iterates can continue going up or down, as happens after every return near $\mathcal{C}_b$, in a quasirandom way. For completeness, the manifolds of $\mathrm{vpo}_L$ are also shown (displayed in blue).

This behaviour suggests that, at the successive returns near $W^c_{L_3,C}$, the Poincaré iterates can approach different tori (2D in the phase space) on that centre manifold. That is, a typical mechanism of diffusion thanks to chains of heteroclinic connections of different tori.

But there are also tori (3D for the Hamiltonian flow, 2D for $\mathcal{P}$) close to these manifolds. Among these tori one finds the ones close to the boundary of the practical stability domain for $L_5$, as seen in subsection 4.3. Looking at Figure 19 one checks that they reach values of $\alpha$ very close to 0 (the value of $\alpha$ for $L_3$) up to $z = 0.4$. The iterates can remain for a large number of iterates (say, $10^6$ and even $10^8$ in some tests) close to one of these tori, to one of the tori in the symmetric domain around $L_4$, or even tori which visit a vicinity of both $L_5$ and $L_4$ (with an $(x, y)$ projection of the iterates in $\Sigma$ similar to the red points in Figure 26). The tori are very sticky, see subsection 3.5. As a consequence, the orbit of a point should consists of passages from the vicinity of $W^u$ of one of the IC to the vicinity of the $W^s$ of another IC (or, perhaps, the same one) with long stays near tori of one of the three types described.

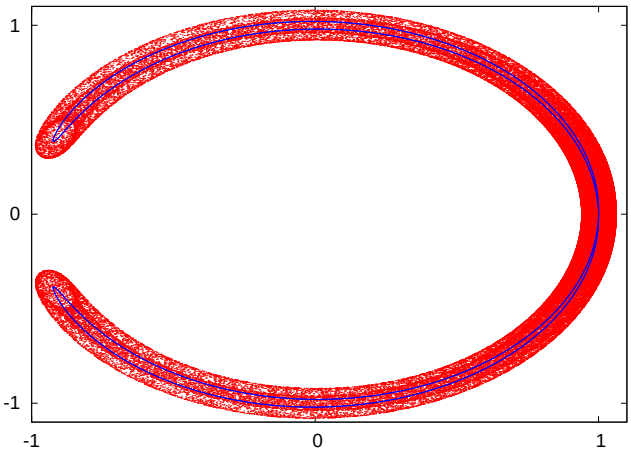


Figure 26: Starting at a point very close to the invariant curve in blue in Figure 25 we have computed the first $10^5$ intersections with $\Sigma$. The plot shows the projections on the $(x, y)$-plane. As a reference we also show in blue the initial part of the manifolds of the $\mathrm{vpo}_L$. The lack of coincidence of these last manifolds is not seen with present resolution.

To have evidence of this expected behaviour, we have taken 1920 points close to $\mathcal{C}_b$ (the blue curve in

Figure 25 left). For every initial point we record the first $5 \times 10^6$ Poincaré iterates, except if some kind of escape is detected. A typical escape occurs when, going the iterates to the left, either near the upper or lower part of Figure 26, they approach the location of the secondary. After this encounter the successive iterates can move close to the primary, escape far away or even return several times near the secondary. Anyway, only for 37 of the 1920 initial conditions escape was detected. Certainly the initial conditions will lead to escape if the number of Poincaré iterates is largely increased, at least on this level of Jacobi constant. See later for some tests with initial data taken near the $\text{vpo}_L$.

To visualize the diffusion and to display a moderate amount of data we have computed passages of the Poincaré iterates through a narrow slice around $x = 0$. Only from time to time an iterate falls in the slice. For instance, among the $1920 \times 5 \times 10^6$ computed Poincaré iterates (except the few iterates lost because of escape) only $\approx 3.2 \times 10^6$ fall in the slice $|x| < 10^{-3}$. The passage can occur in the upper part going from right to left (inner transition) or from left to right (outer transition) and also from right to left (outer transition) or from left to right (inner transition) in the lower part (see Figure 26).

The variables used in $\Sigma$ are $(x, y, \dot{x}, \dot{y})$. Due to the symmetries, the inner upper and inner lower transitions are symmetrical, with the changes $(x, y, \dot{x}, \dot{y}) \leftrightarrow (x, -y, -\dot{x}, \dot{y})$, and the same occurs for the outer ones.

Using only the points falling into the slice up to a maximum of $10^5$ iterates for all the initial conditions, the results (inner and outer upper transitions) are shown in Figure 27 left. The blue points, $P_-$ to the left and $P_+$ to the right, correspond to the intersections with $x = 0$ of the manifolds of the $\text{vpo}_L$. The point $P_-$ is the first intersection of $W^u_{\text{vpo}_L}$ with $x = 0$ and $P_+$ is the first intersection of $W^s_{\text{vpo}_L}$ with $x = 0$. The $y$ coordinate of $P_-$ is smaller than the one of $P_+$. In both cases we refer to the manifolds of $\text{vpo}_L$ as seen in $\Sigma$. Compare with the section through $x = 0$ of the upper part of the blue curves in Figure 26. Note also that in Figure 27 we display $y - 1$ as horizontal coordinate, while $\dot{y}$ is used for the vertical one.

To see the behaviour when the number of iterates increases, the right part of Figure 27 shows the evolution when we consider iterates in the slice after a maximal number of iterations going from $10^5$ to $8 \times 10^5$ and, later, to $5 \times 10^6$ (from green to blue and then to red). The points are plotted in the reverse order. So, blue points hidden red ones and green points hidden blue ones. In magenta we show the location of $P_-$. To prevent from too heavy files we take the narrower slice $|x| < 10^{-4}$ and only show iterates when moving in the upper part to the left, that is, upper inner transitions.

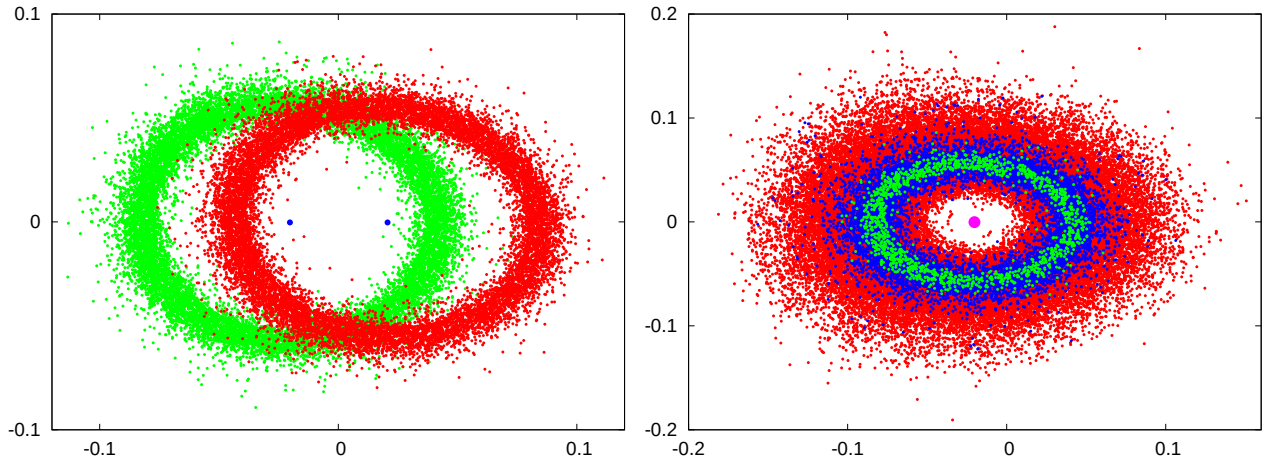


Figure 27: For the set of points described in the text we show the $(y - 1, \dot{y})$ projections using different slices and times, for $y > 0$ (for $y < 0$ it is similar). Left: the slice is defined as $|x| < 10^{-3}$ and we restrict to the first $10^5$ Poincaré iterates of the initial points. In green (resp., red) the points when the iterates move to the left (resp., to the right) when looking at them projected on $(x, y)$. We also show the location of $P_\pm$, as described in the text. Right: Points in the upper inner transitions. In red (resp., blue, green) we plot the points on the slice for a number Poincaré iterates up to $5{\times}10^6$ (resp., up to $8{\times}10^5$, up to $10^5$).

It is interesting to display statistics of the process. A simple measure is the evolution of the distance of the iterates to the point $P_-$, marked in magenta in Figure 27 right. We use the slice $|x| < 10^{-3}$ and all the Poincaré iterates (up to $5 \times 10^6$ for the 1920 initial points, except for 37 points which escape,

after escape is detected). Then we compute the distances $r_{k,i}$ to $P_-$ in the $(y, \dot{y})$ variables, where $i$ is the index of the initial point and $k$ the number of the Poincaré iterate. One takes samples of the $r_{k,i}$ for all the indices $i$ and for ranges of $k$ of the form $((j-1)M, jM], j = 1, \ldots, 100$, with $M = 50,000$. The samples can be labelled by the final value of $k$. The Figure 28 displays, on the left, the behaviour of the average distance as a function of the final value of $k$ in the range of values of $k$ in the sample, while the behaviour of the standard deviation is shown on the right. For these computations both inner transitions (upper and lower) have been taken into account, in order to have larger samples (the total number of inner transitions amounts to 1643007).

The results deserve some discussion. We can consider a diffusion process but, as the rate of diffusion is related to the passage from some 2D torus (invariant curve in the Poincaré section) to a nearby one, from the comments preceding Figure 25, the rate of diffusion is not constant. It increases going away from the $\text{vpo}_L$ and then it decreases again when approaching the $\text{hpo}_L$. From the left plot in Figure 28 it seems that the average is still in a range where the diffusion rate is increasing. This asymmetry is what produces the increase of the average. Note that the value of the distance to $P_-$ for the first iterates which fall in the slice has an average $\approx 0.0597$. Concerning the standard deviation, one should mention that it takes a not so small value ($\approx 0.005$) for $k = 50,000$ (the first displayed point). One of the reasons for this is that, looking at the green points in Figure 27, one checks that they are scattered around an ellipse, not a circle. Also, after 50,000 iterates the scattering is non-negligible.

One can mention that a good fit of the data for the standard deviation, as a function of the number of Poincaré iterates, $k$, is of the form $\sigma \approx c(a_0 + a_1 k + a_2 k^2)^{1/2}$ with $a_0, a_1 > 0, a_2 < 0$ and $c$ a small positive constant. The negative character of $a_2$ should be due to the decrease of the diffusion rate when going to the outer curves in Figure 25.

Furthermore, when the distance $d$ to $P_-$ reaches a value $d^*$ less than, but not too far from 0.18, the orbits quickly escape. One can check that the upper part of the unstable manifold of the $\text{hpo}_L$ has a first intersection with $x = 0$ on a curve, similar to a circle, for which the distance to $P_-$ takes an average value equal to 0.2. Hence, we can consider this as a diffusion process with varying diffusion rate (first increasing, later decreasing, as a function of the distance to $P_-$) and with an absorbing barrier: reaching $d = d^*$ the points disappear from the system.

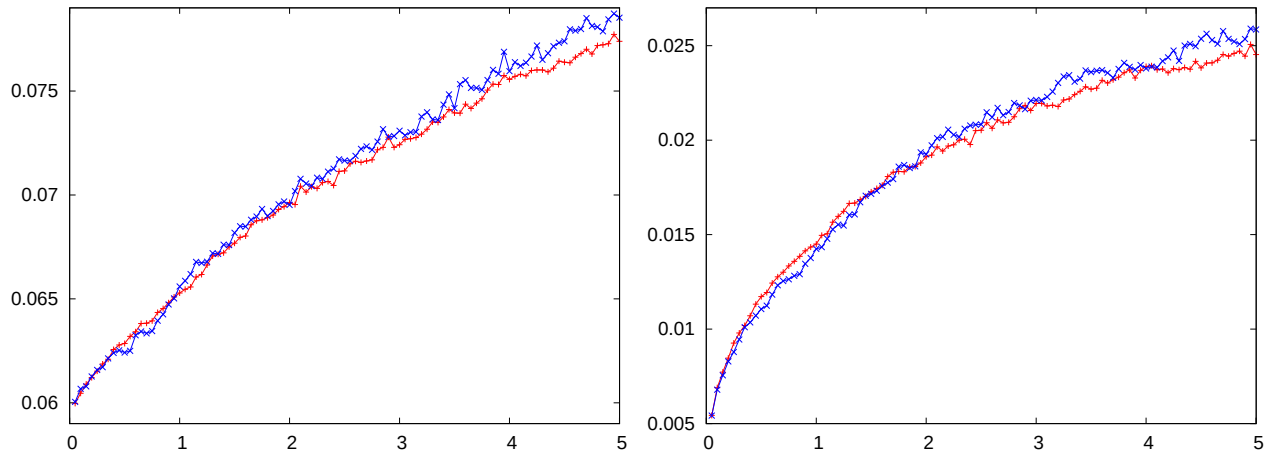


Figure 28: The left (resp., right) plot shows (in red) the evolution of the average (resp., standard deviation) for ranges of $k$ of the form $((j-1)M, jM], j = 1, \ldots, 100$, with $M = 50,000$. The horizontal variable in the plots refers to millions of Poincaré iterates. For comparison, the blue lines show the same results, with a reduced set of initial points, for computations done using quadruple precision. See the text for details.

It is worth to comment also that, as an additional check, preliminary computations concerning diffusion and the related statistics have been carried out using quadruple precision. The size of the sample of initial points has been reduced by a factor 4. The number of escapes before reaching $N = 5 \times 10^6$ is 9, in good agreement with the previous result. Note that now the samples for the statistics are smaller, which gives slightly larger errors in the determination of average and standard deviation. For comparison, the results are displayed in blue also in Figure 28.

Concerning escape, the following experiment has been carried out. A total of 625 initial conditions has been taken in $\Sigma$ at distances of the order of $10^{-13}$ from the intersection of the $\text{vpo}_L$ with $\Sigma$. Poincaré iterates have been computed up to a maximum of $10^9$. The first escape is produced after a number of iterates close to $65 \times 10^5$. Only 13 points subsist for the full $10^9$ iterates, most of them spending a big part of the iterations very close to invariant tori. This is, again, related to the stickiness of these tori. A plot of the number of points which subsist after $k$ iterations, for values of $k$ multiples of $10^7$ is shown in Figure 29.

Furthermore, taking initial data close to the 9 outermost tori in Figure 25 (again using samples of 625 points), one checks that all the points escape and that the average number of iterates for the escape decreases in an exponential way when we approach the outer torus. If the same experiment is done with 625 initial points close to the $\text{hpo}_L$ the result is that all of them escape. In that case, as the orbit lives in $z = 0$, one can count the number of crossings of the orbits through the section $x = 0$, either with $y > 0$ or $y < 0$ and either with $\dot{x} > 0$ or with $\dot{x} < 0$. The average number of such crossings is 14175. Note that, in contrast with the passage of Poincaré iterates through an slice around $x = 0$, it happens that there are outer and inner, upper and lower crossings both with $\dot{x} > 0$ and with $\dot{x} < 0$. See [45] for an explanation of this fact.

These results require a few comments. Up to 64.9 million iterates there is no escape. Only 14 points escape before $10^8$ iterates. Then, up to $\approx 3 \times 10^8$ iterates the number of subsisting points is nearly linear in the number of iterates, that is, a rate of decrease close to a constant. Finally, up to $\approx 9 \times 10^8$ the rate of escape is slightly below an exponential one. The last escape was produced around 870 million iterates. To explain these changes is a *nice open problem*.

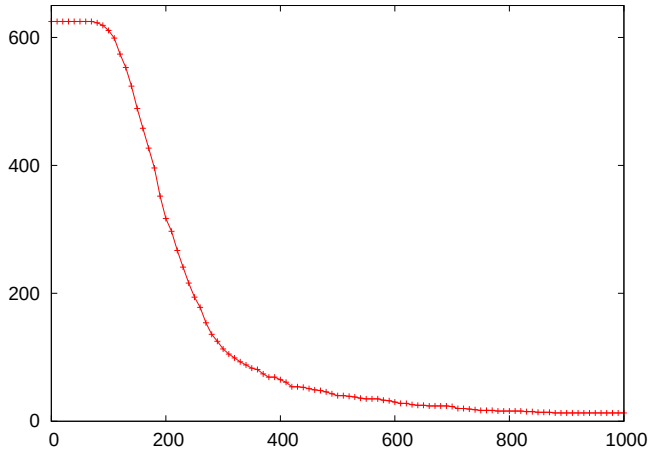


Figure 29: Statistics of the number of non-escaping points, starting close to the $\text{vpo}_L$, as a function of the number of Poincaré iterations. For the simulations one has used a sample of 625 initial points. In the horizontal axis the number of iterations is shown in millions.

A basic ingredient for this application is to have an efficient method to compute Poincaré iterates. Then the steps are:

1) The computation, stability properties and unstable direction of the $\text{vpo}_L$, as fixed point of the Poincaré map, is an easy task. The invariant curves of $\mathcal{P}$ are computed by looking at a representation of the variables $(x, y, \dot{x}, \dot{y})$ as Fourier series in a parametrization angle, using a number of harmonics between 6 and 26, depending on the torus, as explained in subsection 3.3. The symmetries imply that, setting the origin of the angle at the minimal value of $x$, both $x$ and $\dot{y}$ are even, while $y$ and $\dot{x}$ are odd. In this way the left plot in Figure 25 has been obtained. As a side comment we remark that the rotation numbers are of the order of $10^{-4}$ and decreasing when going away from the $\text{vpo}_L$. This produces some problems in the condition number of the linear systems to be solved in the Newton iterations.

2) Next step is the computation of invariant unstable/stable manifolds of the invariant curves. The reversibility implies that it is enough to compute the unstable ones, the stable being then recovered by the symmetries.

We recall that the manifolds have a parametrization as a function of an angle and a distance to the curve. A fundamental domain is diffeomorphic to a cylinder. Looking for points such that after some number of iterations are on an hyperplane $\Pi$ requires a continuation method (e.g., to have the starting distance as a function of the angle) or any similar device. This has been used for the right plot in Figure 25. The plots in Figure 26 follow immediately from the computation of Poincaré iterates.

3) To produce Figure 27 only requires the computation of Poincaré iterates, detection of the passage through a given slice and whether an inner or outer, upper or lower passage occurs. These are elementary tasks, despite the computational cost is high. The statistics can be produced by elementary means.

Note that the difficulties mentioned in item 1), about the smallness of the rotation number, could be expected a priori. The problem in this region of the phase space is a tiny perturbation of the two-body problem in synodical coordinates. If $\mu \to 0$ the limit is the two-body problem, without the singularities which occur in the case of $L_1$ and $L_2$ due to the presence of the secondary, which lead, under suitable scaling, to a limit non-integrable case which is Hill's problem, see [44, 32]. Hence, for $\mu \to 0$ the rotation numbers of the IC like the ones in Figure 25 tend to zero. Concretely, they are $\mathcal{O}(\mu)$, in contrast with the hyperbolicity at $L_3$ and also on the IC, the $\mathrm{vpo}_L$ and the $\mathrm{hpo}_L$ which is $\mathcal{O}(\sqrt{\mu})$. The possible resonances are of a so high order that they become undetectable. The diffusion comes only from the effect of the heteroclinic connections of the manifolds of these IC. The situation is more complex if there is also a relevant amount of hyperbolicity in the centre manifold itself. See related topics in [13].

Summarizing: one has good evidence of the existence of diffusion associated to the centre manifold of $L_3$ on levels of the Jacobi constant not too far from the value at that point. Certainly one can produce escape, due to the effect of the secondary and even for $\mu$ as small as 0.0002, but the escape time is large. Anyway, there are many topics which require further research.

# References


[1] I. Baldomà, À. Haro, One dimensional invariant manifolds of Gevrey type in real-analytic maps. *Discrete Contin. Dyn. Syst. Ser. B* **10** no. 2-3, 295–322 (2008).

[2] X. Cabré, E. Fontich, R. de la Llave, The parameterization method for invariant manifolds. I. Manifolds associated to non-resonant subspaces. *Indiana Univ. Math. J.* **52** no. 2, 283–328 (2003).

[3] X. Cabré, E. Fontich, R. de la Llave, The parameterization method for invariant manifolds. I. Regularity with respect to parameters. *Indiana Univ. Math. J.* **52** no. 2, 329–350 (2003).

[4] X. Cabré, E. Fontich, R. de la Llave, The parameterization method for invariant manifolds. I. Overview and applications. *J. Differential Equations* **218** no. 2, 444–515 (2005).

[5] A. Chenciner, R. Montgomery, A remarkable periodic solution of the three-body problem in the case of equal masses. *Ann. of Math.* (2) **152**, no. 3, 881–901 (2000).

[6] A. Chenciner, J. Gerver, R. Montgomery, C. Simó, Simple Choreographic Motions of $N$ Bodies: A Preliminary Study. In *Geometry, Mechanics and Dynamics*, P. Newton, P. Holmes, A. Weinstein, editors, pp. 287–308, Springer-Verlag, 2002.

[7] B. V. Chirikov, A universal instability of many-dimensional oscillator systems. *Phys. Rep.* **52**, no. 5, 264–379 (1979).

[8] P. M. Cincotta, C. M. Giordano, C. Simó, Phase space structure of multidimensional systems by means of the Mean Exponential Growth factor of Nearby Orbits. *Physica D* **182** 151–178 (2003)

[9] A. Delshams, P. Gutiérrez, Effective stability and KAM theory. *J. Differential Equations* **128** (1996) no. 2, 415–490 (1996).

[10] E. Fontich, C. Simó, Invariant Manifolds for Near Identity Differentiable Maps and Splitting of Separatrices. *Ergod. Th. & Dynam. Sys.* **10** 319–346 (1990).

[11] E. Fontich, C. Simó, The Splitting of Separatrices for Analytic Diffeomorphisms. *Ergod. Th. & Dynam. Sys.* **10** 295–318 (1990).

[12] V. Gelfreich, C. Simó, High-precision computations of divergent asymptotic series and homoclinic phenomena. *Discrete and Continuous Dynamical Systems B* **10** 511–536 (2008).

[13] V. Gelfreich, C. Simó, A. Vieiro, Dynamics of $4D$ symplectic maps near a double resonance. *Physica D* **243** 92–110 (2013).

[14] G. Gómez, A. Jorba, J. Masdemont, C.Simó, *Dynamics and Mission Design Near Libration Points. Volume 3: Advanced Methods for Collinear Points*. World Sci. Pub., Monograph Ser. Math. Vol. 4, Singapore, xiv+187 pp., 2000.

[15] G. Gómez, A. Jorba, J. Masdemont, C.Simó, *Dynamics and Mission Design Near Libration Points. Volume 4: Advanced Methods for Triangular Points*. World Sci. Pub., Monograph Ser. Math. Vol. 5, Singapore, xii+262 pp., 2000.

[16] G. Gómez, J. Llibre, R. Martínez, C.Simó, *Dynamics and Mission Design Near Libration Points. Volume 1: Fundamentals: The Case of Collinear Libration Points*. World Sci. Pub., Monograph Ser. Math. Vol. 2, Singapore, xx+442 pp., 2001.

[17] G. Gómez, J. Llibre, R. Martínez, C.Simó, *Dynamics and Mission Design Near Libration Points. Volume 2: Fundamentals: The Case of Triangular Libration Points*. World Sci. Pub., Monograph Ser. Math. Vol. 3, Singapore, xii+146 pp., 2001.

[18] J. M. Greene, A method for determining stochastic transition. *J. Math. Phys.*, **6** no. 20, pp. 1183–1201 (1976).

[19] M. Hénon, Numerical study of quadratic area-preserving mappings. *Quart. Appl. Math.* **27** 291–312 (1969).

[20] M. Hénon, C. Heiles, The applicability of the third integral of motion: Some numerical experiments. *Astronomical J.* **69** 73–79 (1964).

[21] À. Jorba, E. Olmedo, On the computation of reducible invariant tori on a parallel computer. *SIAM J. Appl. Dyn. Syst.* **8** no. 4, 1382–1404 (2009).

[22] À. Jorba, Maorong Zou, A software package for the numerical integration of ODEs by means of high-order Taylor methods. *Experiment. Math.* **14** no. 1, 99–117 (2005).

[23] T. Kapela, C. Simó, Computer assisted proofs for nonsymmetric planar choreographies and for stability of the Eight. *Nonlinearity* **20** 1241–1255 (2007).

[24] F. Ledrappier, M. Shub, C. Simó, A. Wilkinson, Random versus deterministic exponents in a rich family of diffeomorphisms. *J. Stat Phys.* **113** 85–149 (2003).

[25] R. McGehee, A stable manifold theorem for degenerate fixed points with applications to celestial mechanics. *J. Differential Equations* **14** 70–88 (1973).

[26] R. S. MacKay, A renormalisation approach to invariant circles in area-preserving maps. *Physica D*, **7** no. 1-3, 283–300 (1983).

[27] R. S. MacKay, *Renormalisation in area-preserving maps*. Advanced Series in Nonlinear Dynamics, 6. World Scientific. 1992.

[28] J. Mather, Minimal measures. *Comment. Math. Helv.* **64** 375–394 (1989).

[29] J. Mather, Action minimizing invariant measures for positive definite Lagrangian systems. *Math. Z.* **207** 169–207 (1991).

[30] C. Moore, Braids in Classical Gravity. *Physical Review Letters* **70**, 3675–3679 (1993).

[31] J. J. Morales, J.P. Ramis, C. Simó, Integrability of Hamiltonian Systems and Differential Galois Groups of Higher Variational Equations. *Annales Sci. de l'ENS* $4^e$ série, **40** 845–884 (2007).

[32] J. J. Morales, C. Simó, S. Simón, Algebraic proof of the non-integrability of Hill's Problem. *Ergodic Theory and Dynamical Systems*, **25**, 1237–1256 (2005).

[33] A. Neishtadt, The separation of motions in systems with rapidly rotating phase. *J. Appl. Math. Mech.* **48** 133–139 (1984).

[34] N. N. Nekhorosev, An exponential estimate of the time of stability of nearly-integrable Hamiltonian systems. it Russian Mathematical Syrveys **32** no. 6, 1–65 (1977).

[35] A. Olvera, C. Simó, An obstruction method for the destruction of invariant curves. *Physica D* **26** 181–192 (1987).

[36] J. Sánchez, M. Net, C. Simó, Computation of invariant tori by Newton-Krylov methods in large-scale dissipative systems, *Physica D* **239** 123–133 (2010).

[37] C. Simó, Analytical and numerical computation of invariant manifolds. In *Modern methods in celestial mechanics*, D. Benest and C. Froeschlé, editors, pp. 285–330, Editions Frontières, 1990.

[38] C. Simó, Averaging under fast quasiperiodic forcing. In Proceedings of the NATO-ARW *Integrable and chaotic behaviour in Hamiltonian Systems, Torun, Poland, 1993*, I. Seimenis, editor, pp. 13–34, Plenum Pub. Co., New York, 1994.

[39] C. Simó, Effective Computations in Celestial Mechanics and Astrodynamics. In *Modern Methods of Analytical Mechanics and their Applications*, V.V. Rumyantsev and A. V. Karapetyan, editors, CISM Courses and Lectures **387**, 55–102, Springer, 1998.

[40] C. Simó, Invariant Curves of Perturbations of Non Twist Integrable Area Preserving Maps. *Regular and Chaotic Dynamics* **3** 180–195 (1998).

[41] C. Simó, New families of Solutions in $N$–Body Problems. In *Proceedings of the 3rd European Congress of Mathematics*, C. Casacuberta, R. M. Miró-Roig, J. Verdera, S. Xambó, editors, *Progress in Mathematics series, Vol 201*, 101–115, Birkäuser, Basel, 2001.

[42] C. Simó, Dynamical properties of the figure eight solution of the three-body problem. In *Proceedings of the Celestial Mechanics Conference dedicated to D. Saari for his 60th birthday, Evanston, 1999*, A. Chenciner et al, editors, *Contemporary Mathematics 292*, 209–228, AMS, 2000.

[43] C. Simó, Some properties of the global behaviour of conservative low dimensional systems. In *Foundations of Computational Mathematics: Hong Kong 2008*, F. Cucker et al. editors, pp. 163–189, London Math. Soc. Lecture Notes Series **363**, Cambridge Univ. Press, 2009.

[44] C. Simó, T. Stuchi, Central Stable/Unstable Manifolds and the destruction of KAM tori in the planar Hill problem. *Physica D* **140** 1–32 (2000).

[45] C. Simó, P. Sousa-Silva and M. Terra, Practical Stability Domains near $L_{4,5}$ in the Restricted Three-Body Problem: Some preliminary facts. In *Progress and Challenges in Dynamical Systems*, Vol. 54, Springer, 2013, 367-382.

[46] C. Simó, D. Treschev, Stability islands in the vicinity of separatrices of near-integrable symplectic maps. *Discrete and Continuous Dynamical Systems B* **10** 681–698 (2008).

[47] C. Simó, C. Valls, A formal approximation of the splitting of separatrices in the classical Arnold's example of diffusion with two equal parameters, *Nonlinearity* **14** 1707–1760 (2001).

[48] C. Simó, A. Vieiro, Resonant zones, inner and outer splittings in generic and low order resonances of Area Preserving Maps. *Nonlinearity* **22** 1191–1245 (2009).

[49] C. Simó, A. Vieiro, Dynamics in chaotic zones of area preserving maps: close to separatrix and global instability zones. *Physica D* **240** 732–753 (2011).

**Some classical books**:

V. I. Arnold, *Les méthodes mathématiques de la mécanique classique*. Éditions Mir, Moscow, 1976.
V. I. Arnold, A. Avez, *Problèmes ergodiques de la mécanique classique*. Gauthier-Villars, Paris 1967.
M. W. Hirsch, C. C. Pugh, M. Shub, *Invariant Manifolds*. Lecture Notes in Mathematics, Vol. 583, Springer-Verlag, Heidelberg, 1977.

J. K. Moser, *Stable and random motions in Dynamical Systems: with special emphasis on Celestial Mechanics*, Princeton University Press, Princeton, 1973.
C. L. Siegel, J. K. Moser, *Lectures on celestial mechanics*. Die Grundlehren der mathematischen Wissenschaften, Band 187. Springer-Verlag, New York-Heidelberg, 1971.

**Slides of several talks**:

1. `http://www.maia.ub.es/dsg/2007/` number 8, Taylor method for the integration of ODE.
2. `http://www.maia.ub.es/dsg/2008/` number 3, Some properties of the global behaviour of conservative low dimensional systems.
3. `http://www.maia.ub.es/dsg/2010/` number 4, On the role of Dynamical Systems in Celestial Mechanics.
4. `http://www.maia.ub.es/dsg/2012/` number 8, Domains of Practical Stability near L4,5 in the 3D Restricted Three-Body Problem.
5. `http://www.maia.ub.es/dsg/2013/` number 5, Quadratic Area Preserving Maps in R2.
6. `http://www.maia.ub.es/dsg/2013/` number 7, The dances of the N bodies.
7. `http://www.maia.ub.es/dsg/2013/` number 8, The role of Michel Hénon in detecting regular and chaotic dynamics in conservative systems.